Cancer Cell

Article

Coagulation factor X promotes resistance to androgen-deprivation therapy in prostate cancer

Graphical abstract

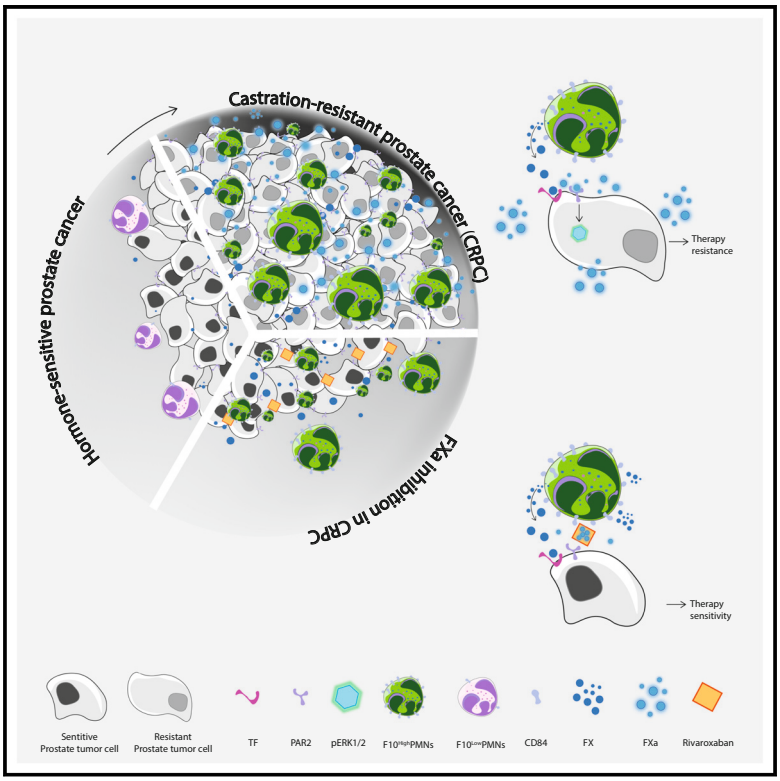

Authors

Bianca Calì, Martina Troiani, Silvia Bressan, ..., Wolfram Ruf, Johann de Bono, Andrea Alimonti

Correspondence

andrea.alimonti@ior.usi.ch

In brief

Calì et al. demonstrate that CD84^{+} immunosuppressive PMNs release in the tumor microenvironment of castration-resistant prostate cancer the coagulation factor X (FX). FX promotes androgen-independent cell proliferation and therapy resistance, independently from the coagulation cascade, by binding PAR2 on prostate cancer cells. This research reveals a new interplay between coagulation factors, immune cells, and cancer.

Highlights

- PMNs are a key source of coagulation factor X (FX) in the tumor microenvironment
- PMN-derived FX directly fuels tumor growth and CRPC
- CD84 marks *F10^{high}Cxcr2^{low}* PMNs in CRPC
- High FX, CD84, and PAR2 levels predict poorer survival in PCa patients

Calì et al., 2024, Cancer Cell *42*, 1676–1692
October 14, 2024
https://doi.org/10.1016/j.ccell.2024.08.018

CellPress

CellPress
OPEN ACCESS

Cancer Cell

Article

Coagulation factor X promotes resistance to androgen-deprivation therapy in prostate cancer

Bianca Calì,[1,2] Martina Troiani,[1,2] Silvia Bressan,[1,2,3] Giuseppe Attanasio,[1,2] Sara Merler,[1,2,4,5,6] Viola Moscarda,[1,2,4] Simone Mosole,[1,2] Elena Ricci,[1,2,7] Christina Guo,[8] Wei Yuan,[8] Lewis Gallagher,[8] Arian Lundberg,[8] Ilona Bernett,[8] Ines Figueiredo,[8] Rydell Alvarez Arzola,[1,9] Ernesto Bermudez Abreut,[1,9] Mariantonietta D'Ambrosio,[1,2] Nicolò Bancaro,[1,2] Daniela Brina,[1,2] Sara Zumerle,[6,10] Emiliano Pasquini,[1,2] Martino Maddalena,[1,2] Ping Lai,[1,2] Manuel Colucci,[1,2] Nicolò Pernigoni,[1,2] Andrea Rinaldi,[1,2] Davide Minardi,[6,11] Alessandro Morlacco,[11] Fabrizio Dal Moro,[11] Marianna Sabbadin,[6,12] Francesca Galuppini,[12] Matteo Fassan,[12] Jan Hendrik Rüschoff,[13] Holger Moch,[13] Pasquale Rescigno,[14] Edoardo Francini,[5,15] Calogero Saieva,[16] Mikol Modesti,[5] Jean-Philippe Theurillat,[1,2] Silke Gillessen,[2,5] Petra Wilgenbus,[17,18] Claudine Graf,[17,18] Wolfram Ruf,[17,18] Johann de Bono,[8] and Andrea Alimonti[1,2,5,6,10,19,20,*]

[1]Institute of Oncology Research (IOR), 6500 Bellinzona, Switzerland
[2]Università della Svizzera Italiana, Faculty of Biomedical Sciences, CH6900 Lugano, Switzerland
[3]Department of Pharmaceutical and Pharmacological Sciences, University of Padova, 35122 Padova, Italy
[4]Section of Oncology, Department of Medicine, University of Verona, 37134 Verona, Italy
[5]Medical Oncology Unit, Oncology Institute of Southern Switzerland, Ente Ospedaliero Cantonale, CH6500 Bellinzona, Switzerland
[6]Veneto Institute of Molecular Medicine, 35129 Padova, Italy
[7]Department of Pharmacy, Health and Nutritional Sciences, University of Calabria, 87036 Rende, Italy
[8]The Institute of Cancer Research, The Royal Marsden Hospital, London SW3 6JJ, UK
[9]Department of Immunoregulation, Immunology and Immunotherapy Division, Center of Molecular Immunology, La Habana 3GGH+C9G, Cuba
[10]Department of Medicine, University of Padova, 35121 Padova, Italy
[11]Urology Clinic, Department of Surgery, Oncology and Gastroenterology, University of Padova, 35128 Padova, Italy
[12]Department of Medicine, Surgical Pathology Unit, University of Padova, 35121 Padova, Italy
[13]Department of Pathology and Molecular Pathology, University Hospital Zurich (USZ), 8091 Zurich, Switzerland
[14]Candiolo Cancer Institute, FPO-IRCCS, 10060 Candiolo, Turin, Italy
[15]Department of Experimental and Clinical Medicine, University of Florence, 50121 Florence, Italy
[16]Cancer Risk Factors and Lifestyle Epidemiology Unit – ISPRO, 50139 Florence, Italy
[17]Center for Thrombosis and Hemostasis, Johannes Gutenberg University Medical Center, 55131 Mainz, Germany
[18]Department of Immunology and Microbiology, Scripps Research, La Jolla, CA 92037, USA
[19]Department of Health Sciences and Technology (D-HEST) ETH Zurich, 8092 Zurich, Switzerland
[20]Lead contact
*Correspondence: andrea.alimonti@ior.usi.ch
https://doi.org/10.1016/j.ccell.2024.08.018

SUMMARY

Although hypercoagulability is commonly associated with malignancies, whether coagulation factors directly affect tumor cell proliferation remains unclear. Herein, by performing single-cell RNA sequencing (scRNA-seq) of the prostate tumor microenvironment (TME) of mouse models of castration-resistant prostate cancer (CRPC), we report that immunosuppressive neutrophils (PMN-MDSCs) are a key extra-hepatic source of coagulation factor X (FX). FX activation within the TME enhances androgen-independent tumor growth by activating the protease-activated receptor 2 (PAR2) and the phosphorylation of ERK1/2 in tumor cells. Genetic and pharmacological inhibition of factor Xa (FXa) antagonizes the oncogenic activity of PMN-MDSCs, reduces tumor progression, and synergizes with enzalutamide therapy. Intriguingly, *F10*^{high} PMN-MDSCs express the surface marker CD84 and CD84 ligation enhances *F10* expression. Elevated levels of FX, CD84, and PAR2 in prostate tumors associate with worse survival in CRPC patients. This study provides evidence that FXa directly promotes cancer and highlights additional targets for PMN-MDSCs for cancer therapies.

INTRODUCTION

Prostate cancer (PCa) is the second most frequent cancer diagnosis made in men and the fifth leading cause of death worldwide.[1] Since PCa initiation and disease progression are driven by androgen receptor (AR) signaling, several effective AR signaling inhibitors (ARSIs) have been developed in the last few years. However, despite initial clinically significant therapy

responses, PCa patients invariably progress to metastatic castration-resistant prostate cancer (mCRPC).[2]

mCRPC are defined as immunologically "cold" tumors largely unresponsive to immune checkpoint inhibitors,[3] partially due to the accumulation of immunosuppressive myeloid cells,[4] driving chronic inflammation[5] often accompanied by enhanced coagulation.[6,7] We previously reported that the intratumor accumulation of CD11b$^+$ Ly6G$^+$ Ly6C^{low} myeloid cells, also known as polymorphonuclear myeloid-derived suppressor cells (PMN-MDSCs) or immunosuppressive neutrophils, drives the onset of castration resistance in multiple mouse models of PCa through IL23-mediated paracrine signaling.[4] We recently identified HGF, SPP1, and BGN as the key tumor secreted factors regulating PMN-MDSCs infiltration and T cells suppression.[8] Of note, intratumor PMN-MDSCs recruitment can be decreased by the administration of a CXCR2 antagonist in *Pten* null prostate conditional (*Pten*$^{pc-/-}$) mice, consequently enhancing the efficacy of both chemotherapy and androgen-deprivation therapy (ADT).[8–10]

mCRPC patients commonly show a high neutrophil-lymphocyte ratio (NLR), a biomarker associated with systemic myeloid inflammation and immunosuppression, which portends a negative prognosis.[11] We recently provided clinical evidence that the administration of the CXCR2 inhibitor AZD5069 plus enzalutamide in a subset of patients with mCRPC progression despite ARSIs treatment reduces intratumor infiltration of CD11b$^+$HLA-DR^{lo}CD15$^+$CD14$^-$ PMN-MDSCs and associates with a significant downregulation of AR activity signatures, eventually increasing patients' disease-free survival.[12] However, in both mouse models and patients affected by mCRPC, inhibition of PMN-MDSCs does not lead to durable responses.

Here, by using single-cell RNA sequencing (scRNA-seq), we report the identification of a subset of CD84$^+$ CD11b$^+$ Ly6G$^+$ Ly6C^{low} immunosuppressive PMNs that secreted the coagulation factor X (FX) into the prostate TME to directly promote PCa growth. FX is a vitamin K-dependent coagulation factor of the blood coagulation cascade,[13] synthesized as a zymogen in the liver and secreted into the bloodstream.[14] FX occupies a central position in the coagulation system, as both the intrinsic and extrinsic pathways of the coagulation cascade converge on its activation.[15] Rapid and localized conversion of FX into its enzymatically active form, factor Xa (FXa), occurs by proteolytic cleavage by either the transmembrane protein tissue factor (TF) complexed with FVIIa, or the activation by FVIIIa/FIXa. Once activated, FXa, in complex with its cofactor FVa, catalyzes the cleavage of prothrombin (FII) to thrombin (FIIa) to eventually promote the formation of insoluble fibrin clots.[16]

Beyond its central role in blood clotting, FXa is synthesized by immune and other cells[17] and elicits cell signaling in extravascular milieus by proteolytically activating the G protein-coupled protease-activated receptor 2 (PAR2). PAR2 activation by TF-FVIIa induces tumor cell signaling[18] and ERK-dependent immune cell migration,[19] whereas FXa-dependent PAR2 activation is implicated in inflammation and innate immune responses.[20,21]

Intriguingly, several evidence demonstrates a tight relationship between venous thromboembolism (VTE) and cancer.[22,23] However, whether coagulation factors directly cause tumor growth remains poorly understood.[24] Here, we find that PMN-derived FXa supported androgen-independent prostate tumor growth by paracrine activation of PAR2 expressed on prostate tumor cells, leading to the emergence of therapy resistance in different mouse models of PCa.

RESULTS

Tumor-infiltrating PMNs upregulate *F10* in CRPC

Immunosuppressive PMNs, characterized in mice by the expression of CD11b$^+$ Ly6G$^+$ Ly6C^{low} markers, represent the major myeloid subset recruited into prostate tumors, particularly in mice and patients resistant to castration.[4,8,10] We previously demonstrated that CXCR2 inhibition or anti-IL-23 antibody treatment can reverse neutrophil-driven CR and enhance the efficacy of enzalutamide in different mouse models of PCa.[4] However, secondary resistance to these treatments eventually emerges, probably due to the secretion of additional factors that support androgen-independent PCa growth.

To identify additional soluble factors upregulated by immunosuppressive PMNs in CRPC, we investigated the secretome of CD11b$^+$ Ly6G$^+$ Ly6C^{low} cells within two tumor models with varying genetic backgrounds, growth rates, and driver mutations. The models used were the *Pten*$^{pc-/-}$ transgenic mouse model, featuring a conditional deletion of the *Pten* allele driven by a Probasin (Pb) promoter and Cre recombinase expression,[25] and the TRAMP-C1 murine cell line, derived from the TRAMP mouse model.[26] We performed scRNA-seq of *Pten*$^{pc-/-}$ and TRAMP-C1 tumors either sensitive (HS) or resistant to surgical castration (CR) followed by bioinformatic analysis (Figures 1A, 1B, S1A, and S1B). To identify PMNs among the tumor-infiltrating cells, we employed uniform manifold approximation and projection (UMAP) dimensionality reduction analysis and a previously published PMN-MDSCs signature[27] (Figures S1C–S1F). Notably, and in line with our previous findings,[4] the CR phase was accompanied by significant alterations of the PMN secretome when compared to HS phase (Figures 1C, 1D, and S1G).

Next, by performing differential expression analyses, we identified seven secreted factors commonly upregulated in PMNs in both models, namely *F10*, *Cxcl1*, *Cxcl2*, *Thbs1*, *Emilin2*, *Cxcl3*, *and Osm* (Figure 1E). Among them, we found that *F10* was almost exclusively upregulated in PMNs in CRPC as compared with other cells in the TME (Figure 1F). Also, *F10* expression levels in PMNs significantly increased as the disease progressed, being positively associated with the emergence of CRPC (Figures 1G and 1H). More relevant, *F10* was also one of the most upregulated factors identified in PMNs in tumors treated with enzalutamide, the CXCR2 inhibitor AZD5069,[12] and an anti-IL-23 antibody (Figures 1I–1K and S1H–S1M). Intriguingly, we found that prolonged treatment with enzalutamide, either alone or in combination with AZD5069 or an anti-IL-23 antibody, was associated with significant upregulation of *F10* in intratumor PMNs, while there were no consistent changes in the expression levels of the other factors identified. Altogether, these findings demonstrate that CD11b$^+$ Ly6G$^+$ Ly6C^{low} cells from CRPC tumors are a key extrahepatic source of *F10* in the prostate TME.

Local activation of FX requires tumor-derived TF and PMN-expressed FVII in CRPC

As FX can be converted to FXa by proteolytic cleavage by either the extrinsic (TF-FVIIa) or intrinsic (FVIIIa-FIXa) coagulation pathways,[15] we first verified the expression of all the coagulation

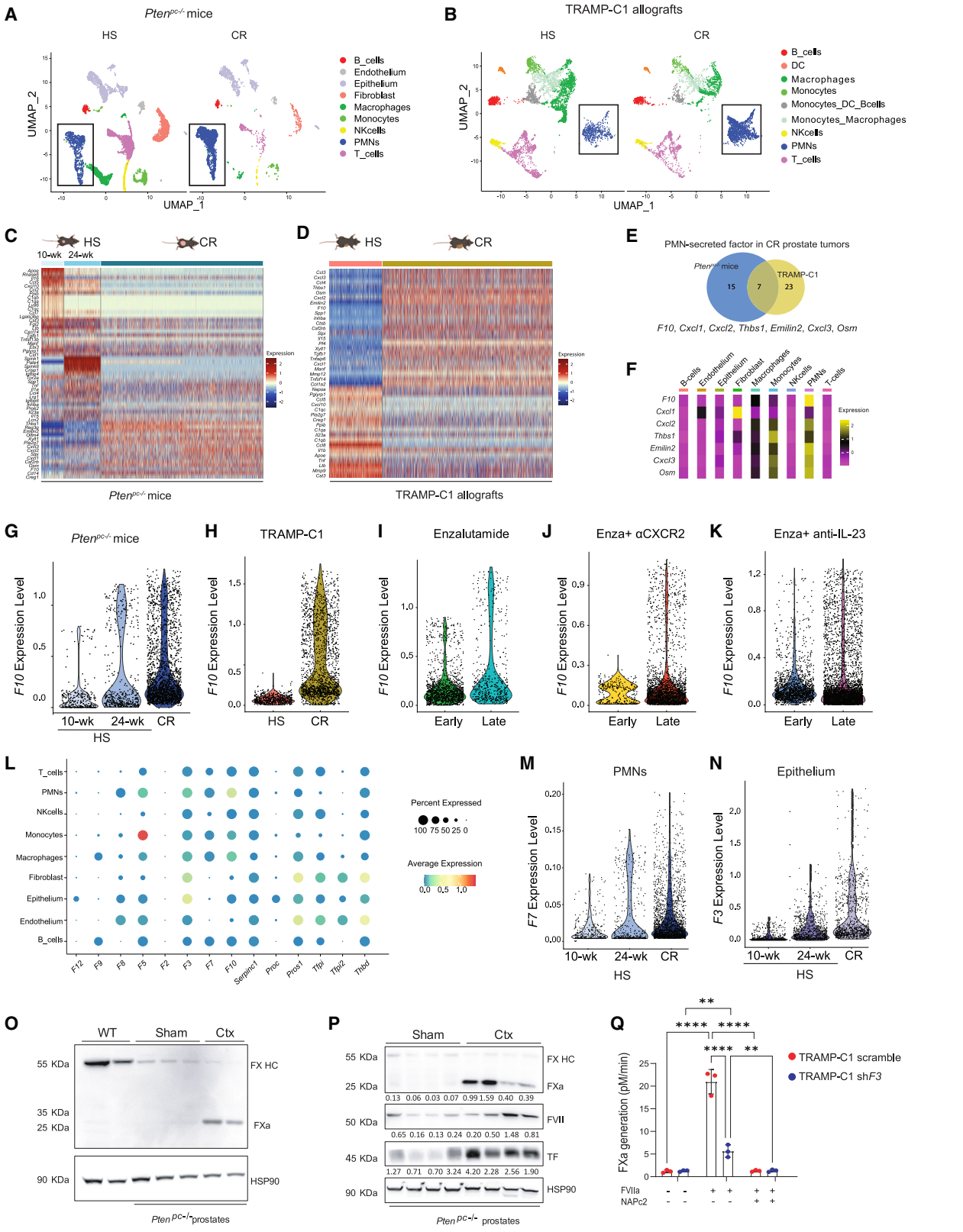

Figure 1. Intratumor PMNs upregulate *F10* in CRPC

(A and B) UMAP of all the integrated datasets identified in *Pten*$^{pc-/-}$ mouse prostates (A) and in TRAMP-C1 allografts (B), either sham-operated (HS) or castration-resistant (CR).

(legend continued on next page)

factors in the TME of CR *Pten*$^{pc-/-}$ prostate tumors by scRNA-seq. We found low to negligible levels of the factors involved in the intrinsic pathway (*F12*, *F9*, and *F8*), and identified the prostate epithelium as the cell subset expressing the highest levels of *F3* in the prostate TME (Figure 1L). Additionally, in *Pten*$^{pc-/-}$ prostates, we found that *F3* and *F7* expression increased with disease progression in epithelial cells and PMNs, respectively, and their levels were even higher in CR phase (Figures 1M and 1N). In line with this evidence, in CR prostate tumors, FX was mainly detectable at lower molecular weight, thus indicating the presence of its cleaved active form (FXa) (Figure 1O). Intriguingly, FXa was only detectable in prostate tumors, but not in plasma samples from CR *Pten*$^{pc-/-}$ mice (Figure S1N), thereby suggesting a critical contribution of the TME in its activation process. Moreover, CR tumors, which were characterized by higher FXa levels, showed increased protein levels of FVII and TF (Figure 1P). To further clarify the mechanism of FX activation in prostate tumors, we performed FXa generation assays *in vitro* by exposing prostate tumor cells to recombinant FX. We found that murine PCa cells required an exogenous FVIIa source to convert FX in FXa, and this process was dependent on TF, as both the pharmacological and genetic blockade of TF reduced FXa generation *in vitro* (Figures 1Q and S1O). Taken together, these data suggest a critical crosstalk between PMNs and the prostate epithelium, which promotes local activation of FX in the proximity of malignant cells.

The intratumor FX-PAR2 axis sustains CRPC

We next assessed whether FXa could directly promote prostate tumor growth by monitoring the proliferation of different prostate tumor cells kept in full-androgen deprivation (FAD).[4] Our results showed that the addition of recombinant FXa to PCa cells kept in FAD was sufficient to promote their androgen-independent cell proliferation both in murine TRAMP-C1 and *Pten*$^{-/-}$; *Trp53*$^{-/-}$ RapidCaP prostate tumor cells[28] (Figures 2A and S2A). These data were also validated with human LNCaP cells kept in FAD (Figure 2B). Note that exposure to FXa *in vitro* increased the growth of prostate tumor cells more than 50% as compared to untreated cells, similarly to IL-23 treatment.

Next, we investigated the mechanism by which FXa drove androgen-independent cell proliferation by looking at the FX binding receptors expressed in PCa cells. Beyond its targets in the coagulation cascade, FXa has been reported to activate epithelial and endothelial cells by cleavage of PAR1 and PAR2.[29] PARs are G-protein coupled receptors (GPCRs) broadly involved in the regulation of platelet function, endothelial permeability, leukocyte adhesion and nitric oxide release, and vascular smooth muscle tension.[30] The four PARs, PAR1–4, are widely expressed in vascular, immune, and epithelial cells and the nervous system. Whereas PAR1, PAR3, and PAR4 are mainly activated by thrombin; PAR2 is activated by trypsin, tryptase, and tissue proteases, as well as by FVIIa and FXa, the two coagulation factors found upregulated in CRPC.[31]

Therefore, to verify the specific targets for FXa activity on prostate tumor cells, we analyzed RNA-seq datasets of either wild-type or *Pten*$^{pc-/-}$ prostates.[8] Differential expression analysis showed that only the *F2rl1* gene, encoding for PAR2, was significantly upregulated in PCa as compared to non-tumoral prostate tissue (Figure 2C). Further bioinformatic analysis of our scRNA-seq data from either HS or CRPC mouse *Pten*$^{pc-/-}$ tumors confirmed the expression of *F2rl1* but did not show relevant expression levels of *F2r* gene, which encodes for PAR1 protein, in prostate epithelial cells (Figures S2B and S2C). Additionally, *F2rl1* gene was almost exclusively expressed by the epithelial cell subset in the prostate TME, both in HS and CR prostate tumors (Figure S2B), and its epithelial expression further increased as the disease progressed to CRPC (Figure 2D). Consistently, western blotting analysis of four different PCa cell lines confirmed the presence of PAR2 and the absence of PAR1 protein in prostate epithelial cells (Figure S2D). Of note, by analyzing publicly available scRNA-seq datasets from PCa patients,[32] we confirmed that *F2RL1* gene was mainly expressed by tumor cells in the TME, showing lower expression in immune cells and normal epithelial cells (Figure S2E). Tumor-specific *F2RL1* expression was further verified by performing western blotting of PAR2 protein in multiple human PCa cell lines, showing very low/negligible expression of PAR2 in benign prostate hyperplasia (BPH) (Figure S2F).

(C and D) Heatmap of the differentially expressed secreted factors in PMNs from *Pten*$^{pc-/-}$ mouse prostates (10-weeks of age = low PIN, 24-weeks of age = high PIN/invasive adenocarcinoma) (C) and TRAMP-C1 allografts (D) as the disease progresses from HS to CRPC.
(E) PMN-secreted factors upregulated in CR in both models.
(F) Heatmap showing the average expression levels of the commonly upregulated secreted factors in the different cell subsets in CR *Pten*$^{pc-/-}$ tumors.
(G) Violin plot showing the expression levels of *F10* in PMNs from *Pten*$^{pc-/-}$ mouse prostates as the disease progresses to CRPC.
(H) *F10* mRNA levels in PMNs from either HS or CR TRAMP-C1 allografts.
(I) *F10* mRNA levels in PMNs from TRAMP-C1 tumors at either the early phase or the late phase of response to enzalutamide.
(J and K) *F10* mRNA levels in PMNs from TRAMP-C1 tumors at either the early phase or the late phase of response to enzalutamide + αCXCR2 (J) and to enzalutamide + anti-IL-23 antibody (K).
(L) Dot plot showing average expression (color-scaled) of coagulation factors and mediators in each cell cluster in CR *Pten*$^{pc-/-}$ tumors. The dot size reflects the proportion of cells expressing the selected gene.
(M) *F7* mRNA levels in PMNs from *Pten*$^{pc-/-}$ tumors with disease progression.
(N) Expression levels of *F3* in epithelial cells from *Pten*$^{pc-/-}$ tumors with disease progression.
(O) Western blot showing both the FX heavy chain (HC) and the activated fractions (FXa) in prostates from healthy wild-type (WT), sham-operated and castrated (Ctx) *Pten*$^{pc-/-}$ mice. HSP90 was used as loading control (n = 2 for WT, n = 3 for sham, n = 2 for Ctx).
(P) Western blot of FX/FXa, FVII, and TF of *Pten*$^{pc-/-}$ mouse prostates (n = 4 for sham, n = 4 for Ctx). Numbers indicate protein levels normalized to HSP90 per each sample.
(Q) FXa generation from either parental (Scramble) or TF knock-down (sh*F3*) TRAMP-C1 cells kept in FAD and exposed to FX with or without FVIIa, and the TF inhibitor NAPc2. Data in (Q) are represented as mean ± SEM and analyzed using two-way ANOVA followed by Tukey's post-hoc test. Statistical test in (C and D), (G–K), and (M and N), false discovery rate (FDR) < 0.05.
See also Figure S1.

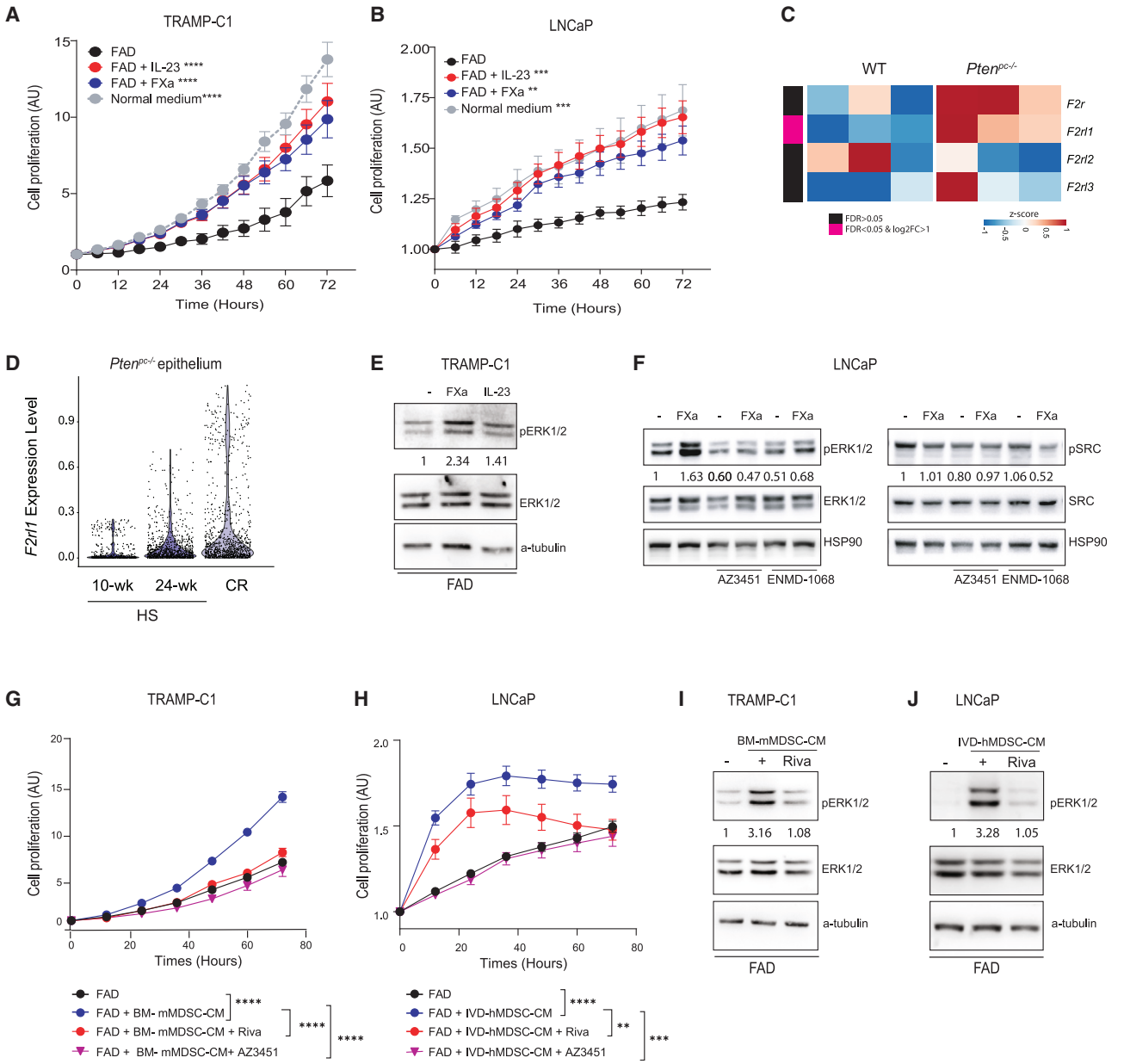

Figure 2. Intratumor FXa-PAR2 axis sustains CRPC

(A and B) Proliferation kinetics of TRAMP-C1 (A) and LNCaP (B) cells kept in FAD and exposed to FXa, IL-23 or optimal culture conditions (normal medium). Results from three independent experiments (mean ± SEM). Two-way ANOVA followed by Dunnett's test.

(C) Heatmap showing the expression levels of *F2r*, *F2rl1*, *F2rl2*, and *F2rl3* in healthy (WT) and *Pten*$^{pc-/-}$ prostates. FDR < 0.05.

(D) Expression levels of *F2rl1* in *Pten*$^{pc-/-}$ prostate epithelium with PCa progression. FDR < 0.05.

(E) ERK1/2 phosphorylation levels in TRAMP-C1 cells kept in FAD and stimulated with either FXa or IL23 as internal control.

(F) Phosphorylation levels of ERK1/2 and SRC kinases in LNCaP cells kept in FAD and stimulated with FXa.

(G and H) Proliferation of TRAMP-C1 (G) and LNCaP (H) cells kept in FAD and exposed to their cognate MDSC-CM. Results from three (G) to four (H) independent experiments (mean ± SEM). Two-way ANOVA followed by Tukey's post-hoc test.

(I and J) ERK1/2 phosphorylation in TRAMP-C1 (I) and LNCaP (J) cells kept in FAD and stimulated with MDSC-CM either alone or in the presence of rivaroxaban (Riva).

See also Figure S2.

Next, we investigated the mechanism by which activated FXa-PAR2 promoted androgen-independent PCa cell proliferation. We exposed PCa cells kept in FAD to recombinant FXa and then probed the cell lysates by western blotting. In both mouse and human PCa cells we found that FXa stimulation induced ERK phosphorylation (pERK1/2) (Figures 2E and 2F), in line with previous findings showing increased pERK1/2 downstream of PAR2 stimulation.[33] To further validate these

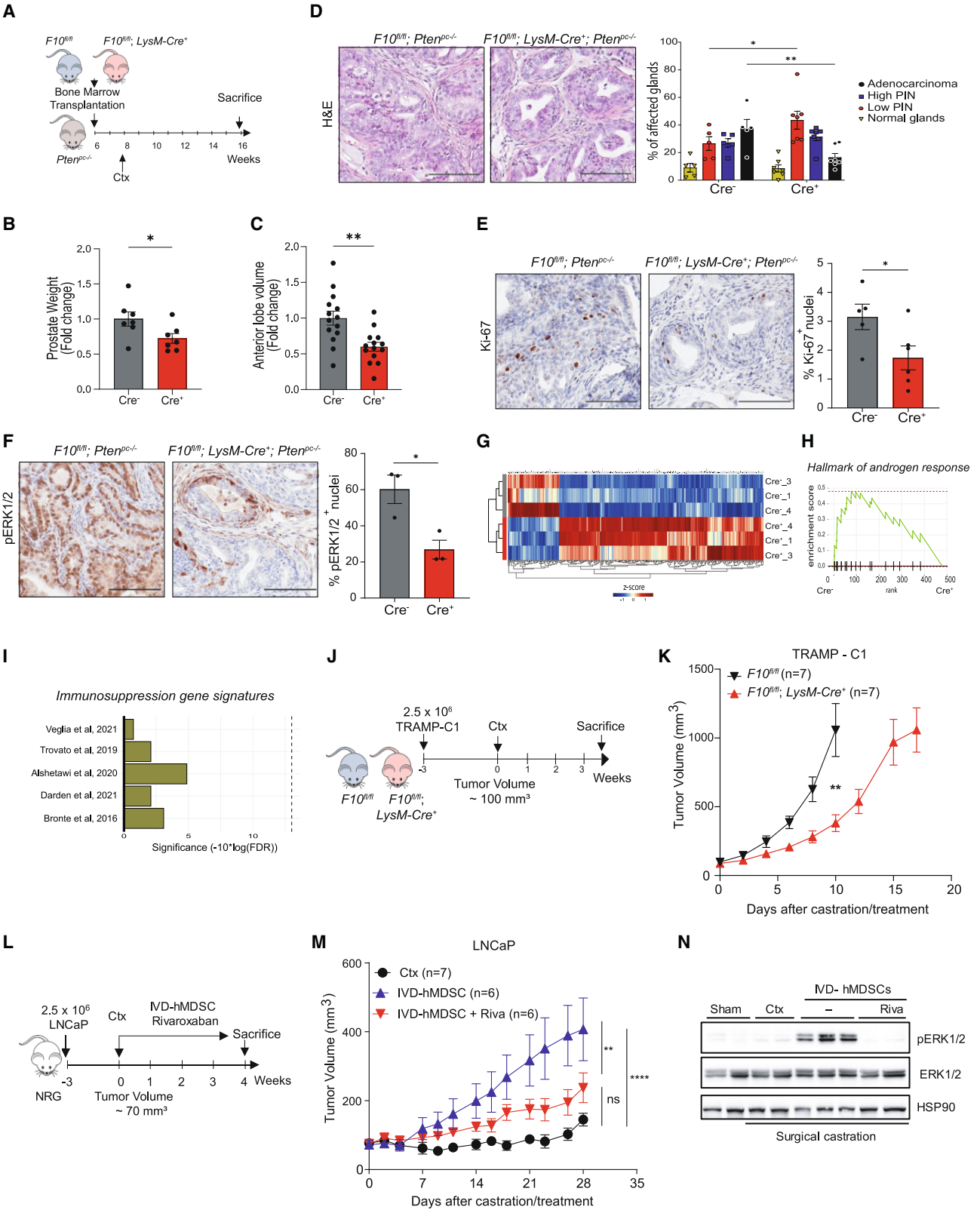

(legend on next page)

results, we performed experiments in the presence of two different PAR2 specific antagonists, AZ3451 and ENMD-1068.[34–36] We found that FXa-triggered ERK phosphorylation was mediated by PAR2 signaling, as it was reduced in the presence of both antagonists (Figure 2F). As PAR2 belongs to the GPCR superfamily, we also tested the effect of either the Gi antagonist pertussis toxin or the protein kinase C inhibitor Go6983 in PCa cells exposed to recombinant FXa. Western blotting analysis showed that FXa-triggered ERK phosphorylation was insensitive to pertussis toxin but required the activity of protein kinase C (PKC) (Figure S2G). Of note, differently from previous results in a breast tumor model,[37] FXa binding to PAR2 did not induce SRC activation in PCa cells (Figure 2F). After validating that both murine and human *in vitro*-generated MDSCs express FX (Figures S2H and S2I), we performed *in vitro* experiments with both TRAMP-C1 and LNCaP cells kept in FAD and treated with the conditioned media of MDSCs (MDSC-CM) in the presence of either AZ3451[34,35] or the FXa inhibitor rivaroxaban (Figures 2G and 2H). While the MDSC-CM induced the proliferation of PCa cells kept in FAD, the specific PAR2 and FXa inhibitors decreased the paracrine oncogenic activity of MDSCs, partially antagonizing ADT resistance (Figures 2G and 2H). FXa inhibition also decreased the proliferation of two different patient-derived prostate organoids (PDOs) treated with the MDSC-CM (Figure S2J). In line with these data, while MDSC-CM increased pERK1/2 in TRAMP-C1 and LNCaP cells, treatment with rivaroxaban strongly abrogated ERK signaling in PCa cells (Figures 2I and 2J). Altogether, these findings provide evidence of the critical role of FXa-PAR2 axis in androgen-independent PCa progression.

PMN-derived FX drives CRPC *in vivo*

To validate these data *in vivo*, we used *F10* $^{fl/fl}$*; LysM-Cre* mice that lack the *F10* gene product in the myeloid cell lineage[17] to generate *Pten*$^{pc-/-}$; *F10*$^{LysM-/-}$ mice deficient for FX synthesis in the myeloid compartment. Upon recovery from bone marrow reconstitution, *Pten*$^{pc-/-}$ mice were either surgically castrated (Ctx) or sham-operated and prostate tumors were analyzed after 8 weeks (Figure 3A). Interestingly, castrated *Pten*$^{pc-/-}$ mice reconstituted with *F10* $^{fl/fl}$*; LysM-Cre*$^{+}$ (Cre^{+}) bone marrow presented significantly smaller tumors as compared with those receiving *F10* $^{fl/fl}$ littermate control (Cre^{-}) bone marrow (Figures 3B and 3C), despite a higher frequency of intratumor neutrophils (Figure S3A). Additionally, prostate glands from castrated *Pten*$^{pc-/-}$ mice reconstituted with *F10* $^{fl/fl}$*; LysM-Cre*$^{+}$ cells showed less aggressive tumors (Figure 3D) and decreased staining for Ki-67 and p-ERK1/2[38] (Figures 3E and 3F). These effects were not seen in *Pten*$^{pc-/-}$; *F10* $^{fl/fl}$*; LysM-Cre* sham-operated mice (Figures S3B–S3D). These results suggest that PMN-derived FX has a critical oncogenic role specifically in castration-resistant settings. Consistently, transcriptomic analysis of tumors from castrated mice showed that *Pten*$^{pc-/-}$; *LysM-Cre*$^{+}$ tumors downregulated the AR signaling when compared to control tumors (Figures 3G, 3H, and S3E). We next assessed whether *F10* deletion in PMN-MDSCs could affect their immunosuppressive functions. Bioinformatic analysis using five different immunosuppressive gene signatures did not show any significant difference in *Pten*$^{pc-/-}$; *F10* $^{fl/fl}$*; LysM-Cre*$^{+}$ tumors as compared to control tumors (Figure 3I). Also, bone marrow derived MDSCs (BM-MDSCs) from either *F10* $^{fl/fl}$ or *F10* $^{fl/fl}$*; LysM-Cre*$^{+}$ mice did not show any significant difference in their immunosuppressive ability (Figure S3F).

To corroborate our findings, we also performed surgical castration of *F10* $^{fl/fl}$ and *F10* $^{fl/fl}$*; LysM-Cre* mice challenged with either TRAMP-C1 or *Ras*$^{+}$*Myc*-induced RM-1[39] mouse PCa cells (Figures 3J and S3G). Interestingly, the kinetics of tumor growth was significantly delayed in castrated *F10* $^{fl/fl}$*; LysM-Cre*$^{+}$ mice compared with control littermates (Figures 3K and S3H). Of note, we found that *F10* mRNA expression levels significantly increased in CD11b^{+} Ly6G^{+} Ly6C^{low} cells infiltrating prostate tumors compared to those from bone marrow (Figure S3I), and that intratumor *F10* $^{fl/fl}$*; LysM-Cre*$^{+}$ PMNs expressed lower *F10* levels as compared with control mice in both models (Figures S3J and S3K). High-dimensional fluorescence-activated cell sorting (FACS) analysis of the tumor immune infiltrate did not show any significant change in the accumulation of immune cell subsets belonging to either the lymphoid

Figure 3. PMN-derived FXa promotes CRPC *in vivo*

(A) Scheme of the experiment with *F10* $^{fl/fl}$*; LysM-Cre; Pten*$^{pc-/-}$ chimeric mice.

(B and C) Whole prostate weights (B) and volumes of the anterior prostate lobes (C) from BM-reconstituted castrated *Pten*$^{pc-/-}$ mice. Student's t test (n = 7 F10 $^{fl/fl}$; *Pten*$^{pc-/-}$ mice, n = 7 *F10* $^{fl/fl}$*; LysM-Cre*$^{+}$; *Pten*$^{pc-/-}$ mice; 2 anterior lobes per mouse were analyzed).

(D) Representative images and relative gland histopathological score of prostates from BM-reconstituted castrated *Pten*$^{pc-/-}$ mice (n = 5 F10 $^{fl/fl}$; *Pten*$^{pc-/-}$ mice, n = 7 *F10* $^{fl/fl}$*; LysM-Cre*$^{+}$; *Pten*$^{pc-/-}$ mice). Two-way ANOVA followed by Sidak's post-hoc test.

(E) Representative images of Ki-67 staining of prostates from BM-reconstituted castrated *Pten*$^{pc-/-}$ mice and relative quantification. Student's t test (n = 5 F10 $^{fl/fl}$; *Pten*$^{pc-/-}$ mice, n = 6 *F10* $^{fl/fl}$*; LysM-Cre*$^{+}$; *Pten*$^{pc-/-}$ mice).

(F) Representative images of phospho-ERK1/2 and relative quantification. Student's t test (n = 3 F10 $^{fl/fl}$; *Pten*$^{pc-/-}$ mice, n = 3 *F10* $^{fl/fl}$*; LysM-Cre*$^{+}$; *Pten*$^{pc-/-}$ mice).

(G) Heatmap of differentially expressed genes between CR tumors from F10 $^{fl/fl}$; *Pten*$^{pc-/-}$ (Cre^{-}) and *F10* $^{fl/fl}$*; LysM-Cre*$^{+}$; *Pten*$^{pc-/-}$ (Cre^{+}) mice.

(H) GSEA querying hallmark genes in mouse CR *Pten*$^{pc-/-}$ tumors, depicting significant enrichment of androgen genes (HALLMARK_ANDROGEN_RESPONSE) in *F10* $^{fl/fl}$; *Pten*$^{pc-/-}$ (Cre^{-}) as compared to *F10* $^{fl/fl}$*; LysM-Cre*$^{+}$; *Pten*$^{pc-/-}$ (Cre^{+}) mice.

(I) Barplot showing immunosuppression signatures in CR tumors from *F10* $^{fl/fl}$; *Pten*$^{pc-/-}$ (Cre^{-}) and *F10* $^{fl/fl}$*; LysM-Cre*$^{+}$; *Pten*$^{pc-/-}$ (Cre^{+}) mice. FDR>0.05.

(J and K) Scheme of the experiment (J) and tumor growth of TRAMP-C1 allografts (K) in either *F10* $^{fl/fl}$ (n = 7) or *F10* $^{fl/fl}$*; LysM-Cre*$^{+}$ (n = 7) castrated mice. Two-way ANOVA followed by Dunnett's multiple comparisons test.

(L and M) Scheme of the experiment (L) and tumor growth of LNCaP xenografts in castrated (Ctx) NRG mice (n = 7) injected with IVD-hMDSCs and treated (n = 6) or not (n = 6) with rivaroxaban (M). Two-way ANOVA followed by Tukey's post-hoc test.

(N) ERK1/2 phosphorylation levels of LNCaP xenografts from either sham or castrated NRG mice injected with IVD-hMDSCs and treated or not with rivaroxaban (n = 2 for sham, n = 2 for Ctx, n = 3 for IVD-hMDSCs, n = 2 for IVD-hMDSCs+ Riva). Plots in (B), (C), (D), (E), (F), (K), and (M) show mean ± SEM. (D, E, and F), scale bar, 100 μm.

See also Figure S3.

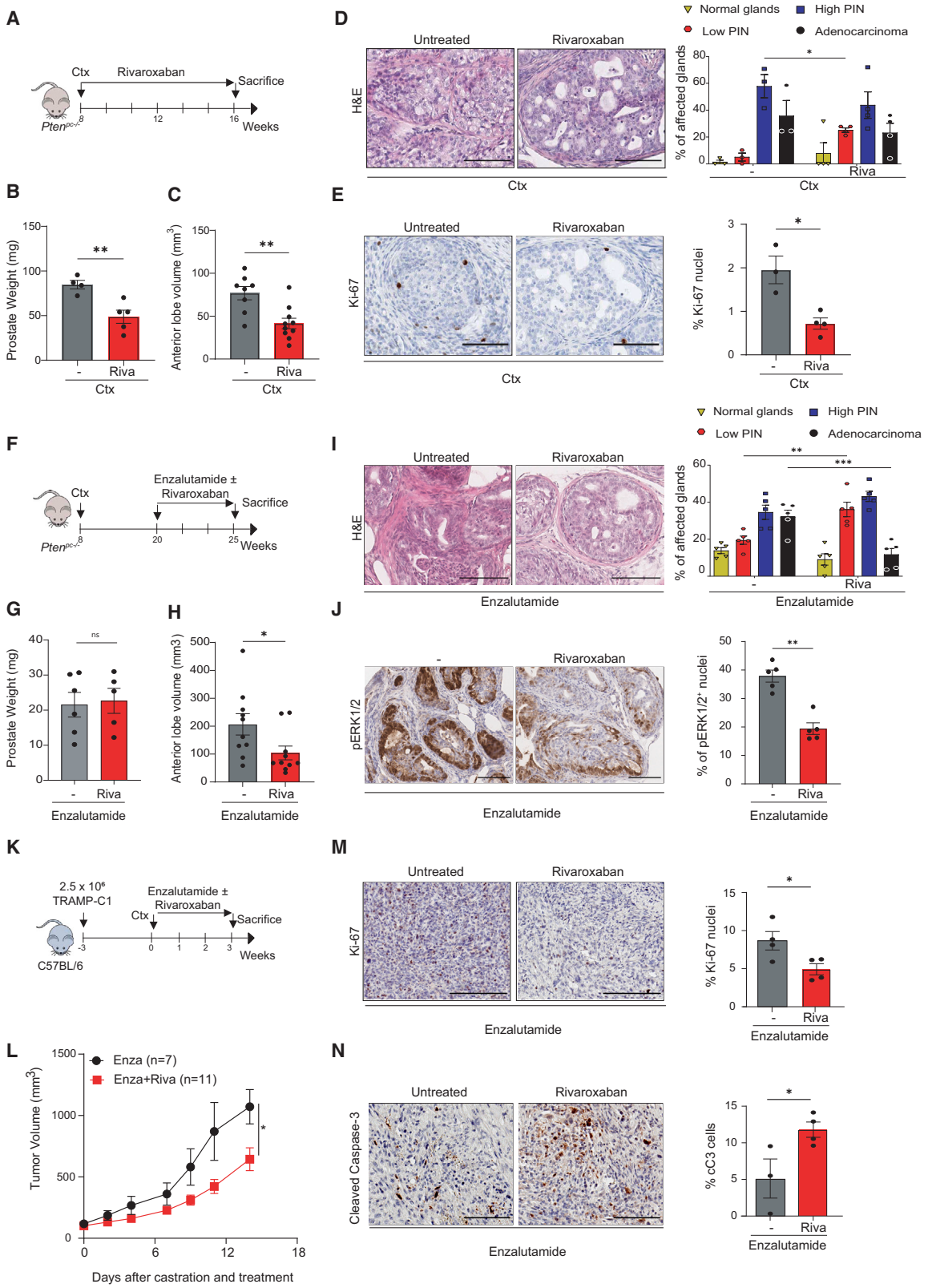

(legend on next page)

or myeloid compartment in the *F10* $^{fl/fl}$*; LysM-Cre*$^{+}$ endogenous mouse model (Figures S3L and S3M). FACS analysis of CR tumors showed that PMNs were the main myeloid source of FX in the TME and that intratumor PMNs from *F10* $^{fl/fl}$*; LysM-Cre*$^{+}$ mice expressed lower levels of FX as compared with control *F10* $^{fl/fl}$ mice (Figures S3N and S3O).

We previously reported that exogenous administration of hMDSCs promotes the onset of CRPC in human PCa xenografts.[4] Therefore, to further validate the role of hMDSCs-derived FX in a human CRPC model, we challenged immunodeficient NRG mice with human LNCaP cells, performed surgical castration when tumors became palpable, and treated the mice with *in vitro*-derived hMDSCs (IVD-hMDSCs), with or without rivaroxaban[40,41](Figure 3L). Of note, despite their immunosuppressive activity *in vitro* (Figures S3P and S3Q), IVD-hMDSC directly supported androgen-independent tumor growth of LNCaP xenografts (Figure 3M). Further, we found that FX inhibition abrogated the oncogenic impact of exogenously administered IVD-hMDSCs, proving the direct involvement of myeloid-derived FX also in human CRPC (Figure 3M). Consistently, treatment with rivaroxaban strongly abrogated ERK signaling in CR LNCaP tumors from mice treated with IVD-hMDSCs (Figure 3N). Taken together, these results provide evidence that myeloid-derived FX has a direct role in PCa biology, which is independent from their immunosuppressive functions, and promotes CRPC growth *in vivo*.

Direct FXa inhibition enhances the efficacy of enzalutamide

Based on our results showing increased intratumor FXa levels in CR settings, we assessed the efficacy of FXa inhibitors in blocking CRPC by treating castrated *Pten*$^{pc-/-}$ mice with rivaroxaban (Figure 4A).[4,42] Intriguingly, we found that prostate tumors from castrated *Pten*$^{pc-/-}$ mice were significantly smaller upon treatment with rivaroxaban than untreated mice (Figures 4B and 4C), despite higher infiltration of PMNs (Figure S4A). Of note, FXa levels were significantly reduced in tumor lysates from rivaroxaban-treated castrated *Pten*$^{pc-/-}$ mice (Figures S4B and S4C). Lower FXa levels also associated with lower numbers of glands affected by aggressive PCa as compared with prostates from untreated mice, decreased percentage of Ki-67^{+} cells (Figures 4D and 4E), and did not impact apoptosis or cellular senescence (Figures S4D–S4G). Interestingly, we did not observe any effect of rivaroxaban treatment on tumor growth, histology, or immune infiltrate in sham-operated mice (Figures S4H–S4K).

The efficacy of FXa inhibition was also validated by challenging C57BL/6 mice with either the TRAMP-C1 (Figures S4L and S4M) or RM-1 allografts (Figures S4N and S4O). Of note, administration of low-molecular-weight heparin (LMWH), which requires the natural anticoagulant antithrombin (AT) to indirectly target FXa, did not affect tumor growth of castrated prostate tumor-bearing mice (Figures S4M and S4O). Collectively, these results indicate that direct FXa inhibitors significantly impact PCa progression, whereas LMWH does not, probably due to the very low levels of AT, encoded by Serpin C1 gene, in the TME and poorer tissue distribution of LMWH when compared to rivaroxaban.[43]

Encouraged by these results, we then investigated whether FXa inhibition could antagonize resistance to ADT in *Pten*$^{pc-/-}$ mice treated with the ARSI enzalutamide, mimicking a clinically relevant scenario. First, we treated mice carrying *Pten*$^{pc-/-}$ tumors with surgical castration; next, we administered enzalutamide either alone or in combination with rivaroxaban (Figure 4F). Analysis of prostates from CR *Pten*$^{pc-/-}$ mice showed that, although not different in weight (Figure 4G), tumors from mice treated with enzalutamide plus rivaroxaban were smaller, less aggressive, and showed reduced pERK1/2 levels, as compared to those receiving enzalutamide alone (Figures 4H–4J). Then, we assessed the efficacy of the combination therapy in castrated TRAMP-C1 allografts (Figure 4K). Our results showed that rivaroxaban in addition to enzalutamide significantly decreased tumor growth when compared with enzalutamide alone (Figure 4L). Combination treatment also decreased the percentage of Ki-67^{+} cells and increased cleaved caspase3 (Figures 4M and 4N) when compared with enzalutamide alone. A similar effect was observed in the RM-1 model (Figure S4P), where administration of enzalutamide plus rivaroxaban significantly delayed tumor

Figure 4. Direct FXa inhibition enhances the efficacy of enzalutamide

(A) Scheme of the experimental setting to verify the efficacy of FXa inhibitors in castrated *Pten*$^{pc-/-}$ mice.

(B and C) Whole prostate weights (B) and volumes of the anterior lobes (C) from castrated *Pten*$^{pc-/-}$ mice treated with rivaroxaban or left untreated (–). (n = 4 control, n = 5 for Riva; 2 anterior lobes per mouse were analyzed).

(D) Representative images of *Pten*$^{pc-/-}$ prostate tumors stained with H&E and relative gland histopathological score (n = 3 control, n = 4 for Riva).

(E) Representative images of tumors stained for Ki-67 and quantification of Ki-67^{+} nuclei (n = 3 control, n = 4 for Riva).

(F) Scheme of the experimental setting to verify the efficacy of FXa inhibitor in antagonizing resistance to enzalutamide in *Pten*$^{pc-/-}$ mouse model.

(G and H) Whole prostate weights (G) and volumes of the anterior lobes (H) from castrated *Pten*$^{pc-/-}$ mice treated with enzalutamide ± rivaroxaban (n = 6 mice treated with Enza, n = 5 mice for Enza+Riva: 2 anterior lobes per mouse were analyzed).

(I) Representative images of H&E staining and gland scoring of prostate tumor slides from *Pten*$^{pc-/-}$ mice treated with enzalutamide ± rivaroxaban (n = 5 for Enza, n = 5 for Enza+Riva).

(J) Representative images of pERK1/2 staining and relative quantification in castrated *Pten*$^{pc-/-}$ mice treated with enzalutamide ± rivaroxaban (n = 5 for Enza, n = 5 for Enza+Riva).

(K and L) Experimental scheme (K) and tumor growth of TRAMP-C1 allografts (L) in castrated C57BL6/N mice treated with enzalutamide ± rivaroxaban (n = 7 for Enza, n = 11 for Enza+Riva).

(M) Representative images and quantification of Ki-67 positive nuclei in TRAMP-C1 allografts from castrated mice either treated with enzalutamide ± rivaroxaban (n = 4 for Enza, n = 4 Enza+Riva).

(N) Representative images and quantification of cleaved Caspase3 (cC3) positive cells in TRAMP-C1 allografts from castrated mice either treated with enzalutamide ± rivaroxaban (n = 3 for Enza, n = 4 Enza+Riva). (D, E, I, M, and N), scale bar, 100 μm. (J), scale bar, 50 μm. (B, C, E, G, H, J, M, and N), plots showing mean ± SEM. Student's t test. (D, I, and L), plots showing mean ± SEM. Two-way ANOVA followed by Sidak's post-hoc test.

See also Figure S4.

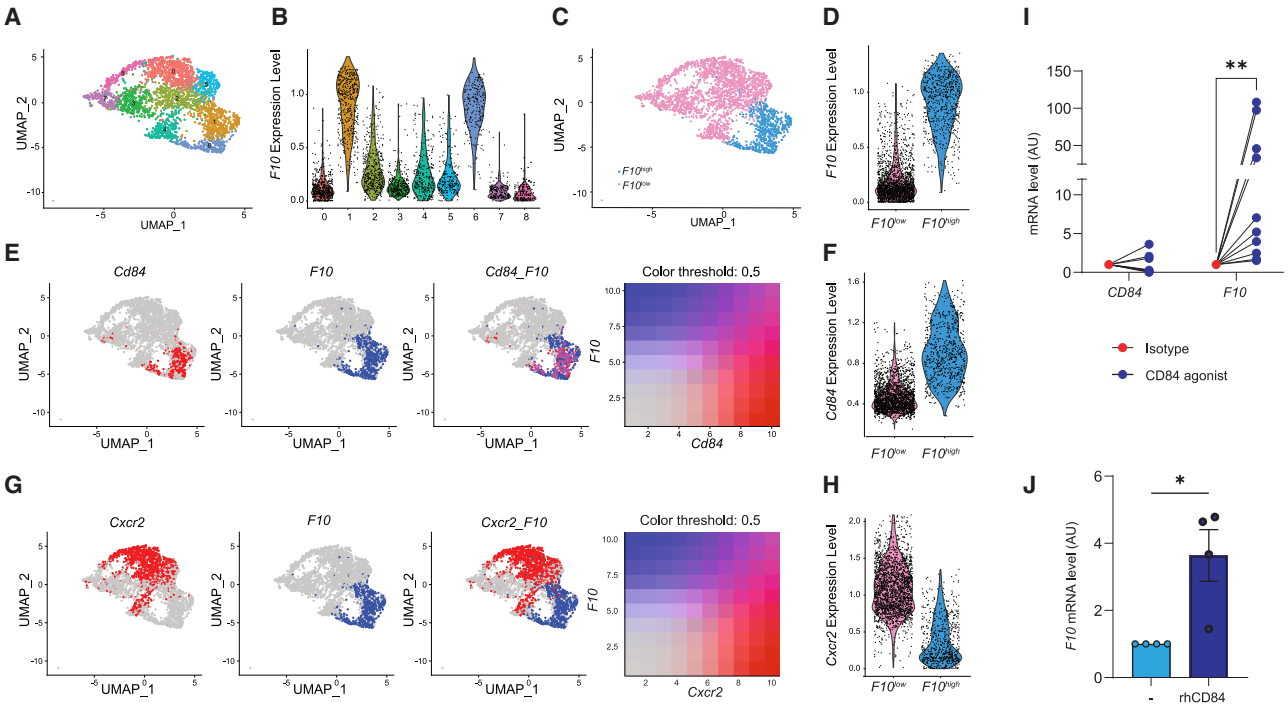

Figure 5. CD84 is a cell surface marker for *F10*^{high} PMNs

(A) UMAP view of the nine PMNs clusters identified in *Pten*$^{pc-/-}$ mouse prostates colored by sample origin (either HS or CR) and by inferred cluster identity.

(B) mRNA expression levels of *F10* in the nine intratumor PMNs clusters from *Pten*$^{pc-/-}$ mice.

(C and D) UMAP plot (C) and violin plot (D) showing the classification of PMNs based on *F10* expression levels in CR *Pten*$^{pc-}$ prostate tumors.

(E) Feature plots showing the co-expression of *Cd84* and *F10* in the PMN clusters from *Pten*$^{pc-/-}$ mice.

(F) Expression levels of *Cd84* in *F10*^{high} and *F10*^{low} PMN subsets from *Pten*$^{pc-/-}$ mouse prostates.

(G) Feature plots showing the co-expression of *Cxcr2* and *F10* in the PMN clusters from *Pten*$^{pc-/-}$ mice.

(H) Expression levels of *Cxcr2* in *F10*^{high} and *F10*^{low} PMN subsets from *Pten*$^{pc-/-}$ mouse prostates.

(I) qRT-PCR analyses of the indicated genes in IVD-hMDSCs stimulated with either an anti-CD84 antibody (CD84 agonist) or isotype control. Plot shows means ± SEM. (n = 9 independent experiments). Two-way ANOVA test, followed by Sidak's post-hoc test.

(J) qRT-PCR analyses of *F10* in IVD-hMDSCs stimulated with recombinant human CD84. Plot shows means ± SEM (n = 4 independent experiments). Mann-Whitney test. (A–H), FDR < 0.05.

See also Figure S5.

growth (Figure S4Q). Taken together, these results provide evidence that direct FXa inhibitors can antagonize resistance to ADT and enhance the efficacy of enzalutamide in PCa.

F10^{high} PMNs express the cell surface marker CD84 and are *Cxcr2*^{low}

To further characterize the *F10*^{high} PMNs in CRPC, we performed differential expression analysis of the transmembrane proteins significantly upregulated in the *F10*^{high} PMNs as compared with *F10*^{low} (Figure S5A). We found that *Cd84* was significantly enriched in *F10*^{high} PMNs and positively correlated with *F10* in PMNs from CR *Pten*$^{pc-/-}$ mouse prostates (Figures 5A–5F). Of note, PMNs showed the highest expression level of *Cd84* as compared with other cells in the TME (Figure S5B).

CD84 (SLAMF5) is a pan-leukocyte cell surface molecule,[44] that establishes homophilic interactions to support prolonged T cell:B cell contact, optimal T follicular helper function, and germinal center formation for efficient antibody production.[45] Recently, CD84 was described as a phenotypic marker of immunosuppressive myeloid cells in multiple myeloma and breast cancer.[46–48] In line with these findings, FACS analysis of human prostate adenocarcinoma confirmed CD84 expression in tumor infiltrating myeloid cells (Figure S5C). We found that both *Cd84* and *F10* expression were increased in BM-MDSCs differentiated under ADT *in vitro* (Figure S5D). Intriguingly, *Cd84*$^{+}$, *F10*^{high} PMNs were also characterized by low expression levels of *Cxcr2* (Figures 5G and 5H). These data were further validated in intratumor PMNs from castration-resistant TRAMP-C1 tumor bearing mice (Figure S5E). These *F10*^{high} *Cxcr2*^{low} PMNs identified in CRPC mouse tumors were not characterized by gene expression signatures of either aged or senescent-like neutrophils, but they rather showed lower expression of genes related to neutrophil maturation (Figure S5F).[10,49–52] Further bioinformatic analysis of *F10*^{high} *Cxcr2*^{low} PMNs indicated that, despite a lower *Cxcr2* mRNA expression, this cell subset expressed higher levels of several genes associated with leukocyte intrinsic cell motility, cytokinesis, and *trans*-endothelial migration, including *Bsg*, *Gna13*, *Plgrkt*, and *Alcam* (Figure S5G).[53–56] Taken together, these findings suggest the existence of an aggressive PMNs subset in CRPC with lower sensitivity to CXCR2 inhibitors. To investigate whether CD84 was functionally associated with *F10*, we used IVD-hMDSCs,

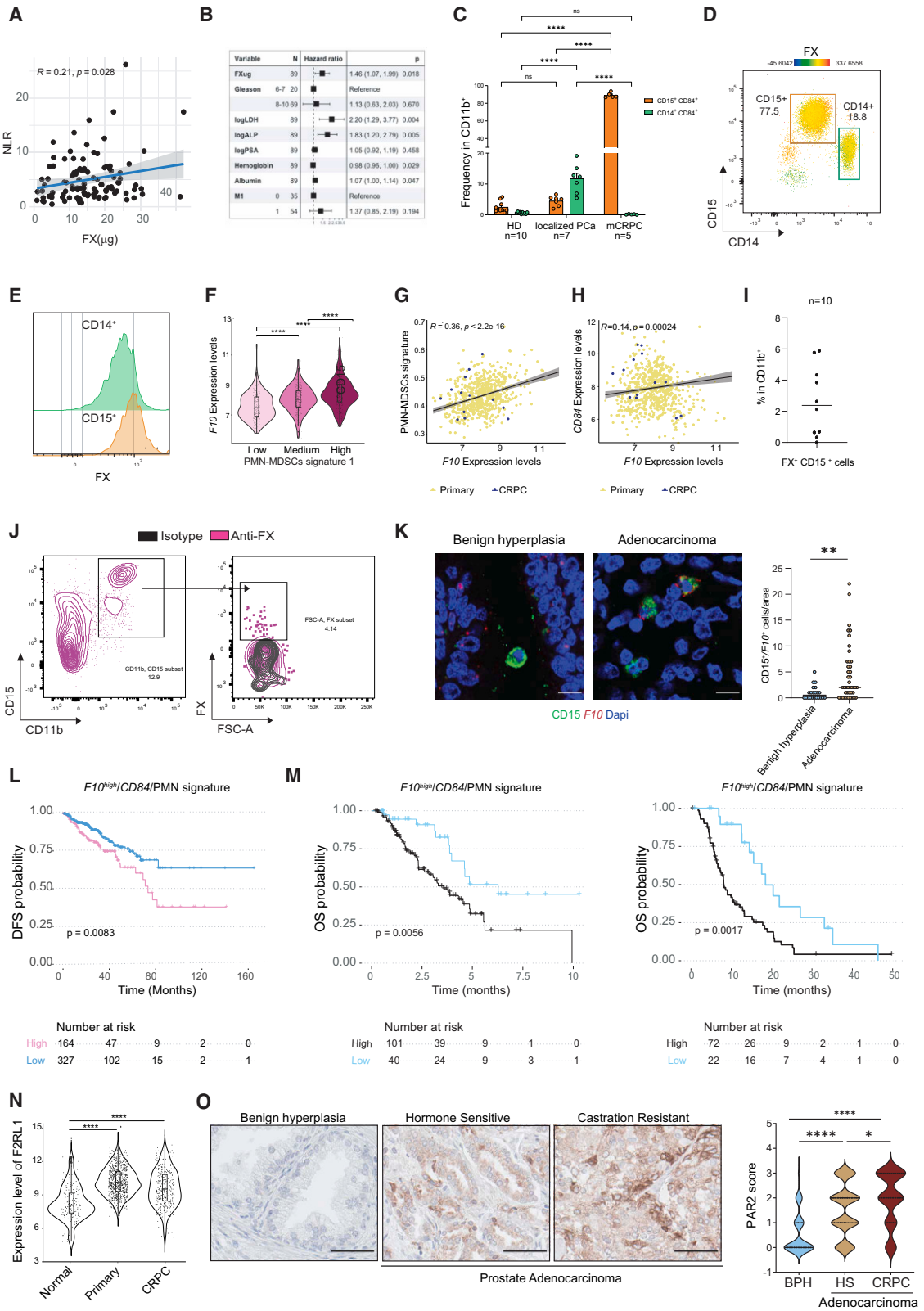

Figure 6. A *F10*^{high}*/CD84*/PMN signature is prognostic of worse disease in PCa patients

(A) Pearson's correlation between NLR and FX (µg) plasma levels in mCRPC patients (n = 106; R = 0.21; p = 0.028).

(B) Multivariable-Cox regression analysis for 89 mCRPC patients. Hazard ratio for FX (µg) is calculated for per 10 µg change in serum FX levels.

(legend continued on next page)

which express both CD33 and CD84 markers *in vitro* (Figure S5H), as a model to assess the effect of CD84 ligation on *F10* expression. Hence, we stimulated IVD-hMDSCs with an activating anti-CD84 antibody.[47] Interestingly, we found that exposure to a CD84 agonist enhanced the expression levels of *F10*, without significantly affecting *CD84* expression *in vitro* (Figure 5I). These data were further validated by stimulating IVD-hMDSCs with a recombinant human CD84 protein (Figure 5J). We next looked at the promoter sequence of *F10* and we found an IRF8 binding site located 1.6 kb from the transcription start site. We therefore checked by western blotting IRF8 levels in cells stimulated with CD84 agonist and found that IRF8 levels were strongly upregulated upon CD84 ligation (Figure S5I). These results, in line with previous chromatin immunoprecipitation sequencing (ChIP-seq) data showing high binding scores for IRF8 in the *F10* gene promoter region,[57] suggest that CD84 ligation induces *F10* expression by stabilizing IRF8 protein. Altogether, these data demonstrate a strong association between CD84 activation and the upregulation of *F10* in immunosuppressive myeloid cells.

CD84/F10^{high} PMNs increase in CRPC and are associated with poor survival in PCa patients

We next assessed the relevance of these data on PCa patients. Intriguingly, analyses of data from 106 patients with mCRPC showed that plasma FX level positively associated with NLR (Figure 6A) and peripheral blood neutrophil counts (Figure S6A), and that high plasma FX level was independently prognostic of poorer overall survival (Figure 6B) on multivariate analyses. In line with these findings, FACS analysis of blood from mCRPC patients showed higher FX expression specifically in CD11b$^+$ CD84$^+$ CD15$^+$ cells as compared with CD11b$^+$ CD84$^+$ CD14$^+$ cells (Figures 6C–6E). These results suggested that the increased plasma level of FX was a consequence of the expansion of FX-producing PMNs in CRPC.

Next, we assessed FX levels in human tumor samples. Bioinformatic analysis of a large cohort of more than 600 PCa patients[58] showed that *F10* mRNA levels positively associated with three different PMN-MDSCs signatures[5,51,59] and strongly correlated with *CD84* mRNA levels in human prostate tumor biopsies (Figures 6F–6H and S6B–S6K). FACS analysis of human prostate adenocarcinoma confirmed FX expression in tumor-infiltrating CD15$^+$ cells (Figures 6I and 6J). Additionally, we performed *F10* RNA-*in situ* hybridization (RNA*ish*) on prostate tissues from patients affected by either benign hyperplasia or adenocarcinoma, followed by immunofluorescence for CD15. Our analysis showed that *F10*$^+$/CD15$^+$ myeloid cell numbers were significantly higher in human prostate adenocarcinoma as compared with benign hyperplasia tissue samples, showing a growing trend with higher Gleason scores (Figures 6K and S6L).

Next, to verify that intratumor neutrophil-derived FX was associated with the survival of PCa patients, we generated a *F10^{high}/CD84*/PMN gene signature, which included the canonical markers of PMN-MDSCs, *F10*, *CD84*, and other six genes found to be commonly elevated in the *F10^{high}* PMN subset in human and mouse settings (Figure S6M). By stratifying the patients of the publicly available The Cancer Genome Atlas (TCGA) cohort and two different proprietary mCRPC cohorts for the *F10^{high}/CD84*/PMN gene signature, we found that a high *F10^{high}/CD84*/PMN signature was associated with significantly shorter survival (Figures 6L and 6M). Altogether, these data suggest that the presence of *F10^{high}* myeloid cells in human PCa samples is predictive of worse prognosis.

We next verified the expression of *F2RL1* in human prostate tumor samples. Bioinformatic analysis of the publicly available human PCa tissue datasets[58] showed that *F2RL1* mRNA levels were significantly increased in prostate tumors as compared with healthy prostates (Figure 6N). Further, immunostaining of human prostate tissue microarrays (TMAs) from 79 HS to 71 CRPC patients showed that PAR2 levels increased with tumor progression, being higher in CRPC than in HSPCs and prostate hyperplasia (Figures 6O and S6N). Of note, PAR2 levels were elevated in both primary and metastatic tumor samples from a second cohort of 63 metastatic hormone-sensitive (mHS) patient-matched tumor samples (Figure S6O). Interestingly, and in line with our preclinical results, we found that both *F10* and *F2RL1* mRNA levels correlate with AR activity signature in one out of two human CRPC datasets analyzed (Figure S6P). Finally, analysis of PAR2 staining of human prostate tumors revealed that negative PAR2 scores were associated with a significantly longer disease-free survival in patients with adenocarcinoma (Figure S6Q).

(C) Frequency of CD15$^+$ CD84$^+$ and CD14$^+$ CD84$^+$ cells in peripheral blood of healthy donors (HD, $n = 10$) and patients affected by either localized PCa ($n = 7$) or mCRPC ($n = 5$) patients. Plot showing means ± SEM. Two-way ANOVA, followed by Sidak's post-hoc test.
(D) Representative FACS plot showing FX intensity in circulating CD15$^+$ and CD14$^+$ cells from CRPC patients.
(E) Representative FACS histogram showing FX intensity in circulating CD15$^+$ and CD14$^+$ cells from mCRPC patients.
(F) *F10* expression levels in human PCa stratified based on the PMN-MDSCs signature 1. Two-way ANOVA followed by Tukey's post-hoc test.
(G) Pearson's correlation between the PMN-MDSCs signature 1 and *F10* in human PCa (R = 0.36, $p < 2.2e\text{-}16$).
(H) Pearson's correlation between *CD84* and *F10* in human PCa (R = 0.14, $p = 0.00024$).
(I) Frequency of FX$^+$ CD15$^+$ cells in human PCa biopsies ($n = 10$). Horizontal line in the dot plot represents the median.
(J) Representative FACS plot showing FX positive signal in CD11b$^+$ CD15$^+$ cells in human PCa biopsies.
(K) Representative confocal fluorescence images and counts of *F10* (red)/CD15 (green) positive cells per area analyzed in human benign hyperplasia and adenocarcinoma. Scale bar, 10 μm. Horizontal lines in the dot plot represent medians ($n = 22$ for BPH, $n = 44$ for adenocarcinoma). Mann-Whitney U test. $^{**}p < 0.01$.
(L) Kaplan-Meier curves for disease-free survival in primary PCa sample from TCGA dataset stratified based on the *F10^{high}/CD84*/PMN signature.
(M) Kaplan-Meier curves for overall survival in mCRPC sample from SU2C (*left*, $n = 141$) and RMH cohorts (*right*, $n = 94$) stratified based on the *F10^{high}/CD84*/PMN signature.
(N) *F2RL1* expression levels in human prostate tissues. Two-way ANOVA followed by Tukey's post-hoc test.
(O) Representative images of human prostate TMAs stained for PAR2 and violin plot showing the PAR2 score ($n = 44$ for BPH, $n = 79$ for hormone-sensitive adenocarcinoma and $n = 71$ for CRPC). Scale bar, 50 μm. One-way ANOVA test, followed by Tukey's post-hoc test.
See also Figure S6.

DISCUSSION

The relationship between VTE and cancer was first described in 1865 by Armand Trousseau, who found that tumors promoted coagulation and platelet activation in patients.[22] Pre-clinical studies have reported that coagulation factors can enhance metastasis formation, by activating either endothelial-cancer cell adhesion or migration and invasion.[60–62] Also, the expression of procoagulant factors, including TF, by cancer cells appears to correlate with advanced disease and poor survival in multiple cancer histotypes.[23,63]

Several clinical studies in cancer patients with or without VTE have suggested that LMWH prolongs the overall survival of different cancer patients, with no difference in death related to VTE or bleeding.[64–66] Notably, VTE prophylaxis with warfarin decreased the incidence of different malignancies, particularly PCa, in a large cohort of Swedish patients prospectively followed up for several years.[67] Together, these puzzling clinical observations suggest that coagulation factors have a direct role in tumorigenesis and PCa progression.

Intriguingly, two clinical studies have recently highlighted that the use of ADT associates with a ~80% increased risk of VTE in PCa patients.[68,69] This can be explained by the expansion of circulating PMNs, which is commonly reported in CRPC patients.

The role of neutrophils in promoting thrombosis in inflammatory non-cancer related diseases has been extensively studied.[70] However, the contribution of immunosuppressive PMNs to intravascular coagulation events has been only recently suggested in the context of severe COVID-19.[71]

The discovery that tumor infiltrating PMNs associate with resistance to taxanes[9] and AR signaling inhibitors (ARSIs), such as abiraterone and enzalutamide,[72] in mCRPC patients has prompted the clinical investigation of therapeutic strategies aimed at blocking either their intratumor recruitment (NCT03177187) or their oncogenic functions (NCT04458311). On this line, we recently demonstrated that blocking myeloid chemotaxis can reduce tumor-elicited myeloid inflammation and reverse therapy resistance in a subset of mCRPC patients.[12]

Once inside the tumors, PMNs secrete tumor-promoting factors, including IL-23, by which they drive castration-resistance in PCa.[4] Here, we discovered that PMNs within the prostate TME are a key extrahepatic source of FX, which sustains resistance to ADT.

Intriguingly, we identified CD84 as a key marker of this oncogenic myeloid subset expressing high levels of *F10* in both preclinical and clinical PCa cancer settings. High expression levels of CD84 were previously reported in both intratumor and splenic mouse PMNs showing T cell-suppressive capacity and increased ROS production.[46] In humans, CD84 was found to be expressed by both Mo-MDSCs and PMN-MDSCs, with CD84 co-expressed with LOX1 in PMN-MDSCs.[27] In line with these findings, we proved that *in vitro* ligation of CD84 enhances *F10* expression in IVD-hMDSCs, indicating a functional association between CD84 and *F10* in immunosuppressive cells. Of note, increased CD84 expression levels were found in platelets from COVID-19 and sepsis patients and were associated with poor outcome in a cohort of stroke patients, emphasizing the role of CD84 in thrombo-inflammation.[73,74]

Differently from IL-23, which drives the transcription of AR and downstream target genes via the pSTAT3-RORγ axis,[4] PMN-derived FX triggers tumor growth by activating the ERK pathway in epithelial cancer cells through PAR2. These results indicate a direct role of FX on PCa cell biology, other than the indirect FXa pro-angiogenic and pro-metastatic effects already described for other malignancies.[60–62] Autocrine TF-PAR2 axis in myeloid cells has been shown to promote profibrotic activation in myocardial infarction[75] and macrophage reprogramming in immunologically hot tumors.[17] Here, we show a distinctly different paracrine signaling that is mediated by PMN-released FX and promotes tumor growth despite androgen-deprivation by activation of PAR2 on cancer epithelial cells. Of note, our data demonstrate that immunosuppressive PMNs are the most abundant, and thus relevant, myeloid cell subset producing FX in CR mouse prostate tumors.[4,9]

From a clinical perspective, we demonstrated that elevated plasma levels of FX, as well as a high *F10*^{high}*/CD84*/PMN gene signature on tumor samples associate with worse survival in PCa. Also, while low PAR2 levels in prostate tumor samples are associated with longer disease-free survival, high *F10* and *F2RL1* expression correlate with higher AR signature, thus unveiling an unprecedented prognostic role for FX-PAR2 axis in CRPC patients. Furthermore, we found that administration of specific FXa inhibitors effectively hampers tumor growth in different prostate tumor cells and human organoids and affect CRPC progression in multiple syngeneic and xenograft mouse models. Finally, we proved that FXa inhibition enhances the efficacy of enzalutamide treatment in multiple mouse models of CRPC. Altogether, our results lead the way for the design and exploitation of novel combinatorial strategies targeting the coagulation cascade for the treatment of castration-resistant PCa.

RESOURCE AVAILABILITY

Lead contact

Further information and requests for resources and reagents should be directed to and will be fulfilled by the lead contact, Andrea Alimonti (andrea.alimonti@ior.usi.ch).

Materials availability

All reagents generated in Alimonti's laboratory used in this study are available from the lead contact with a completed materials transfer agreement.

Data and code availability

Single-cell RNA-seq and RNA-seq data generated for this study have been deposited at GEO and are publicly available. GEO accession numbers are listed in the key resources table.

The accession numbers for the other existing, publicly available, scRNA-seq and RNA-seq datasets analyzed for this study are listed in the key resources table.

ACKNOWLEDGMENTS

We thank Daniela Bossi, Daniele Braga, Anna Kohl, Aurora Valdata, Luisa Maraccani, David Jarrossay, Diego Morone, and all the members of the animal core Bios+ facility for their technical and scientific advice. Buffy coats were kindly provided by Dr. Federico Mele and Prof. Federica Sallusto (IRB, Bellinzona, Switzerland). PCa biopsies were provided by Gianmarco Randazzo, Giuseppe Reitano and Filippo Carletti (Urology Clinic, University of Padova, Padova, Italy). RapidCaP cells were provided by Prof. Lloyd C Trotman (Cold Spring Harbor Laboratory). Funding: German Research Foundation (project number

318346496 and SFB1292/2 TP10) (W.R. and C. Graf); PCF-19CHAL08 (A.A.); ISREC Foundation, Fidinam Foundation, and Novartis Foundation for medical-biological Research #21A009 (A.A.); ERC-CoG 683136 (A.A.); SNSF Excellence grant 201274 (A.A.); and SNSF Sinergia grant 202302 (A.A.).

AUTHOR CONTRIBUTIONS

Conceptualization: B.C. and A.A. Methodology: B.C., M.T., C. Guo, W.Y., S. Mosole, M.D.A., E.P., A.R., F.G., P.W., and C. Graf. Investigation: B.C., M.T., S.B., G.A., S. Merler, V.M., S. Mosole, E.R., C. Guo., I.B., I.F., R.A.A., E.B.A., M.D.A., P.L., M.C., N.P., M. Maddalena, M.S., P.W., and C. Graf. Formal analysis: B.C., M.T., S.B., C. Guo, W.Y., L.G., A.L., and M.F. Visualization: B.C., M.T., S.B., E.R., and N.B. Resources: D.B., D.M., A.M., F.D.M., F.G., M.F., J.H.R., H.M., P.R., E.F., C.S., S.Z.., M. Modesti, J.-P.T., S.G., P.W., C. Graf, W.R., and J.d.B. Project administration: B.C. and A.A. Funding acquisition: A.A., W.R., and C. Graf. Supervision: W.R., J.d.B., and A.A. Writing – original draft: B.C. and A.A. Writing – review & editing: B.C., M.T., S.B., S.Z., D.B., C. Guo, W.R., J.d.B., and A.A.

DECLARATION OF INTERESTS

Authors declare no competing interests.

STAR★METHODS

Detailed methods are provided in the online version of this paper and include the following:

- KEY RESOURCES TABLE
- EXPERIMENTAL MODEL AND STUDY PARTICIPANT DETAILS
  - Cell lines
  - Mouse models
  - Human samples
  - *In vitro*-generation of MDSCs and collection of MDSC-CM
  - Cell proliferation assays
  - PDX-O proliferation assay
  - *In vitro* mouse T cell suppression assay
  - *In vitro* human T cell suppression assay
  - Generation of a sh*F3* TRAMP-C1 cells
  - FXa generation assay
  - *In vitro* FXa-PAR2 stimulation
  - *In vitro* CD84 activation
  - qPCR
  - Western blotting
  - *In vivo* treatments
  - Bone marrow reconstitution
  - Bulk RNA-sequencing analysis
  - Single – cell RNA-sequencing analysis
  - *F10*^{high}/CD84/PMN signature
  - Bioinformatic analysis of PCa RNA-seq data
  - Flow cytometry and analysis
  - Immunohistochemistry and immunofluorescence
  - RNAish
  - Quantification of plasma levels of FX in CRPC patients and survival analysis
  - Statistical analysis

SUPPLEMENTAL INFORMATION

Supplemental information can be found online at https://doi.org/10.1016/j.ccell.2024.08.018.

Received: December 6, 2023
Revised: June 13, 2024
Accepted: August 22, 2024
Published: September 19, 2024

REFERENCES

1. Bray, F., Ferlay, J., Soerjomataram, I., Siegel, R.L., Torre, L.A., and Jemal, A. (2018). Global cancer statistics 2018: GLOBOCAN estimates of incidence and mortality worldwide for 36 cancers in 185 countries. CA. Cancer J. Clin. *68*, 394–424. https://doi.org/10.3322/caac.21492.
2. Nuhn, P., De Bono, J.S., Fizazi, K., Freedland, S.J., Grilli, M., Kantoff, P.W., Sonpavde, G., Sternberg, C.N., Yegnasubramanian, S., and Antonarakis, E.S. (2019). Update on Systemic Prostate Cancer Therapies: Management of Metastatic Castration-resistant Prostate Cancer in the Era of Precision Oncology. Eur. Urol. *75*, 88–99. https://doi.org/10.1016/j.eururo.2018.03.028.
3. Subudhi, S.K., Siddiqui, B.A., Aparicio, A.M., Yadav, S.S., Basu, S., Chen, H., Jindal, S., Tidwell, R.S.S., Varma, A., Logothetis, C.J., et al. (2021). Combined CTLA-4 and PD-L1 blockade in patients with chemotherapy-naive metastatic castration-resistant prostate cancer is associated with increased myeloid and neutrophil immune subsets in the bone microenvironment. J. Immunother. Cancer *9*, e002919. https://doi.org/10.1136/jitc-2021-002919.
4. Calcinotto, A., Spataro, C., Zagato, E., Di Mitri, D., Gil, V., Crespo, M., De Bernardis, G., Losa, M., Mirenda, M., Pasquini, E., et al. (2018). IL-23 secreted by myeloid cells drives castration-resistant prostate cancer. Nature *559*, 363–369. https://doi.org/10.1038/s41586-018-0266-0.
5. Bronte, V., Brandau, S., Chen, S.H., Colombo, M.P., Frey, A.B., Greten, T.F., Mandruzzato, S., Murray, P.J., Ochoa, A., Ostrand-Rosenberg, S., et al. (2016). Recommendations for myeloid-derived suppressor cell nomenclature and characterization standards. Nat. Commun. *7*, 12150. https://doi.org/10.1038/ncomms12150.
6. Graf, C., and Ruf, W. (2018). Tissue factor as a mediator of coagulation and signaling in cancer and chronic inflammation. Thromb. Res. *164*, S143–S147. https://doi.org/10.1016/j.thromres.2018.01.023.
7. Galmiche, A., Rak, J., Roumenina, L.T., and Saidak, Z. (2022). Coagulome and the tumor microenvironment: an actionable interplay. Trends Cancer *8*, 369–383. https://doi.org/10.1016/j.trecan.2021.12.008.
8. Brina, D., Ponzoni, A., Troiani, M., Calì, B., Pasquini, E., Attanasio, G., Mosole, S., Mirenda, M., D'Ambrosio, M., Colucci, M., et al. (2023). The Akt/mTOR and MNK/eIF4E pathways rewire the prostate cancer translatome to secrete HGF, SPP1 and BGN and recruit suppressive myeloid cells. Nat. Cancer *4*, 1102–1121. https://doi.org/10.1038/s43018-023-00594-z.
9. Di Mitri, D., Toso, A., Chen, J.J., Sarti, M., Pinton, S., Jost, T.R., D'Antuono, R., Montani, E., Garcia-Escudero, R., Guccini, I., et al. (2014). Tumour-infiltrating Gr-1+ myeloid cells antagonize senescence in cancer. Nature *515*, 134–137. https://doi.org/10.1038/nature13638.
10. Bancaro, N., Cali, B., Troiani, M., Elia, A.R., Arzola, R.A., Attanasio, G., Lai, P., Crespo, M., Gurel, B., Pereira, R., et al. (2023). Apolipoprotein E induces pathogenic senescent-like myeloid cells in prostate cancer. Cancer Cell *41*, 602–619.e11. https://doi.org/10.1016/j.ccell.2023.02.004.
11. Lorente, D., Mateo, J., Templeton, A.J., Zafeiriou, Z., Bianchini, D., Ferraldeschi, R., Bahl, A., Shen, L., Su, Z., Sartor, O., and de Bono, J.S. (2015). Baseline neutrophil-lymphocyte ratio (NLR) is associated with survival and response to treatment with second-line chemotherapy for advanced prostate cancer independent of baseline steroid use. Ann. Oncol. *26*, 750–755. https://doi.org/10.1093/annonc/mdu587.
12. Guo, C., Sharp, A., Gurel, B., Crespo, M., Figueiredo, I., Jain, S., Vogl, U., Rekowski, J., Rouhifard, M., Gallagher, L., et al. (2023). Targeting myeloid chemotaxis to reverse prostate cancer therapy resistance. Nature *623*, 1053–1061. https://doi.org/10.1038/s41586-023-06696-z.
13. Millar, D.S., Elliston, L., Deex, P., Krawczak, M., Wacey, A.I., Reynaud, J., Nieuwenhuis, H.K., Bolton-Maggs, P., Mannucci, P.M., Reverter, J.C., et al. (2000). Molecular analysis of the genotype-phenotype relationship in factor X deficiency. Hum. Genet. *106*, 249–257. https://doi.org/10.1007/s004390051035.

14. Cooper, D.N., Millar, D.S., Wacey, A., Banner, D.W., and Tuddenham, E.G. (1997). Inherited factor VII deficiency: molecular genetics and pathophysiology. Thromb. Haemost. *78*, 151–160.

15. Camire, R.M. (2021). Blood coagulation factor X: molecular biology, inherited disease, and engineered therapeutics. J. Thromb. Thrombolysis *52*, 383–390. https://doi.org/10.1007/s11239-021-02456-w.

16. Grover, S.P., and Mackman, N. (2019). Intrinsic Pathway of Coagulation and Thrombosis. Arterioscler. Thromb. Vasc. Biol. *39*, 331–338. https://doi.org/10.1161/ATVBAHA.118.312130.

17. Graf, C., Wilgenbus, P., Pagel, S., Pott, J., Marini, F., Reyda, S., Kitano, M., Macher-Göppinger, S., Weiler, H., and Ruf, W. (2019). Myeloid cell-synthesized coagulation factor X dampens antitumor immunity. Sci. Immunol. *4*, eaaw8405. https://doi.org/10.1126/sciimmunol.aaw8405.

18. Rothmeier, A.S., Liu, E., Chakrabarty, S., Disse, J., Mueller, B.M., Østergaard, H., and Ruf, W. (2018). Identification of the integrin-binding site on coagulation factor VIIa required for proangiogenic PAR2 signaling. Blood *131*, 674–685. https://doi.org/10.1182/blood-2017-02-768218.

19. Zelaya, H., Grunz, K., Nguyen, T.S., Habibi, A., Witzler, C., Reyda, S., Gonzalez-Menendez, I., Quintanilla-Martinez, L., Bosmann, M., Weiler, H., and Ruf, W. (2024). Nucleic acid sensing promotes inflammatory monocyte migration through biased coagulation factor VIIa signaling. Blood *143*, 845–857. https://doi.org/10.1182/blood.2023021149.

20. Liang, H.P.H., Kerschen, E.J., Hernandez, I., Basu, S., Zogg, M., Botros, F., Jia, S., Hessner, M.J., Griffin, J.H., Ruf, W., and Weiler, H. (2015). EPCR-dependent PAR2 activation by the blood coagulation initiation complex regulates LPS-triggered interferon responses in mice. Blood *125*, 2845–2854. https://doi.org/10.1182/blood-2014-11-610717.

21. Fleischer, M.I., Röhrig, N., Raker, V.K., Springer, J., Becker, D., Ritz, S., Bros, M., Stege, H., Haist, M., Grabbe, S., et al. (2022). Protease- and cell type-specific activation of protease-activated receptor 2 in cutaneous inflammation. J. Thromb. Haemost. *20*, 2823–2836. https://doi.org/10.1111/jth.15894.

22. Noble, S., and Pasi, J. (2010). Epidemiology and pathophysiology of cancer-associated thrombosis. Br. J. Cancer *102*, S2–S9. https://doi.org/10.1038/sj.bjc.6605599.

23. Palumbo, J.S., and Degen, J.L. (2007). Mechanisms linking tumor cell-associated procoagulant function to tumor metastasis. Thromb. Res. *120*, S22–S28. https://doi.org/10.1016/S0049-3848(07)70127-5.

24. Ruf, W. (2021). Roles of factor Xa beyond coagulation. J. Thromb. Thrombolysis *52*, 391–396. https://doi.org/10.1007/s11239-021-02458-8.

25. Lee, Y.R., and Pandolfi, P.P. (2020). PTEN Mouse Models of Cancer Initiation and Progression. Cold Spring Harb. Perspect. Med. *10*, a037283. https://doi.org/10.1101/cshperspect.a037283.

26. Foster, B.A., Gingrich, J.R., Kwon, E.D., Madias, C., and Greenberg, N.M. (1997). Characterization of prostatic epithelial cell lines derived from transgenic adenocarcinoma of the mouse prostate (TRAMP) model. Cancer Res. *57*, 3325–3330.

27. Veglia, F., Perego, M., and Gabrilovich, D. (2018). Myeloid-derived suppressor cells coming of age. Nat. Immunol. *19*, 108–119. https://doi.org/10.1038/s41590-017-0022-x.

28. Cho, H., Herzka, T., Zheng, W., Qi, J., Wilkinson, J.E., Bradner, J.E., Robinson, B.D., Castillo-Martin, M., Cordon-Cardo, C., and Trotman, L.C. (2014). RapidCaP, a novel GEM model for metastatic prostate cancer analysis and therapy, reveals myc as a driver of Pten-mutant metastasis. Cancer Discov. *4*, 318–333. https://doi.org/10.1158/2159-8290.CD-13-0346.

29. Camerer, E., Rottingen, J.A., Iversen, J.G., and Prydz, H. (1996). Coagulation factors VII and X induce Ca2+ oscillations in Madin-Darby canine kidney cells only when proteolytically active. J. Biol. Chem. *271*, 29034–29042. https://doi.org/10.1074/jbc.271.46.29034.

30. Ramachandran, R., Noorbakhsh, F., Defea, K., and Hollenberg, M.D. (2012). Targeting proteinase-activated receptors: therapeutic potential and challenges. Nat. Rev. Drug Discov. *11*, 69–86. https://doi.org/10.1038/nrd3615.

31. Coughlin, S.R. (2000). Thrombin signalling and protease-activated receptors. Nature *407*, 258–264. https://doi.org/10.1038/35025229.

32. Hirz, T., Mei, S., Sarkar, H., Kfoury, Y., Wu, S., Verhoeven, B.M., Subtelny, A.O., Zlatev, D.V., Wszolek, M.W., Salari, K., et al. (2023). Dissecting the immune suppressive human prostate tumor microenvironment via integrated single-cell and spatial transcriptomic analyses. Nat. Commun. *14*, 663. https://doi.org/10.1038/s41467-023-36325-2.

33. Zhou, B., Zhou, H., Ling, S., Guo, D., Yan, Y., Zhou, F., and Wu, Y. (2011). Activation of PAR2 or/and TLR4 promotes SW620 cell proliferation and migration via phosphorylation of ERK1/2. Oncol. Rep. *25*, 503–511. https://doi.org/10.3892/or.2010.1077.

34. Cheng, R.K.Y., Fiez-Vandal, C., Schlenker, O., Edman, K., Aggeler, B., Brown, D.G., Brown, G.A., Cooke, R.M., Dumelin, C.E., Doré, A.S., et al. (2017). Structural insight into allosteric modulation of protease-activated receptor 2. Nature *545*, 112–115. https://doi.org/10.1038/nature22309.

35. Kennedy, A.J., Sundström, L., Geschwindner, S., Poon, E.K.Y., Jiang, Y., Chen, R., Cooke, R., Johnstone, S., Madin, A., Lim, J., et al. (2020). Protease-activated receptor-2 ligands reveal orthosteric and allosteric mechanisms of receptor inhibition. Commun. Biol. *3*, 782. https://doi.org/10.1038/s42003-020-01504-0.

36. Heuberger, D.M., and Schuepbach, R.A. (2019). Protease-activated receptors (PARs): mechanisms of action and potential therapeutic modulators in PAR-driven inflammatory diseases. Thromb. J. *17*, 4. https://doi.org/10.1186/s12959-019-0194-8.

37. Su, S., Li, Y., Luo, Y., Sheng, Y., Su, Y., Padia, R.N., Pan, Z.K., Dong, Z., and Huang, S. (2009). Proteinase-activated receptor 2 expression in breast cancer and its role in breast cancer cell migration. Oncogene *28*, 3047–3057. https://doi.org/10.1038/onc.2009.163.

38. Robinson, D., Van Allen, E.M., Wu, Y.M., Schultz, N., Lonigro, R.J., Mosquera, J.M., Montgomery, B., Taplin, M.E., Pritchard, C.C., Attard, G., et al. (2015). Integrative clinical genomics of advanced prostate cancer. Cell *161*, 1215–1228. https://doi.org/10.1016/j.cell.2015.05.001.

39. Power, C.A., Pwint, H., Chan, J., Cho, J., Yu, Y., Walsh, W., and Russell, P.J. (2009). A novel model of bone-metastatic prostate cancer in immunocompetent mice. Prostate *69*, 1613–1623. https://doi.org/10.1002/pros.21010.

40. Gao, H., Ouyang, X., Banach-Petrosky, W.A., Gerald, W.L., Shen, M.M., and Abate-Shen, C. (2006). Combinatorial activities of Akt and B-Raf/Erk signaling in a mouse model of androgen-independent prostate cancer. Proc. Natl. Acad. Sci. USA *103*, 14477–14482. https://doi.org/10.1073/pnas.0606836103.

41. Liang, B., Liang, Y., Zhao, L.Z., Zhao, Y.X., and Gu, N. (2021). Rivaroxaban for cancer-associated venous thromboembolism. Sci. Prog. *104*, 368504211012160. https://doi.org/10.1177/00368504211012160.

42. Germanos, A.A., Arora, S., Zheng, Y., Goddard, E.T., Coleman, I.M., Ku, A.T., Wilkinson, S., Song, H., Brady, N.J., Amezquita, R.A., et al. (2022). Defining cellular population dynamics at single-cell resolution during prostate cancer progression. Elife *11*. https://doi.org/10.7554/eLife.79076.

43. Carlson, T.H., Simon, T.L., and Atencio, A.C. (1985). In vivo behavior of human radioiodinated antithrombin III: distribution among three physiologic pools. Blood *66*, 13–19.

44. Sintes, J., Romero, X., de Salort, J., Terhorst, C., and Engel, P. (2010). Mouse CD84 is a pan-leukocyte cell-surface molecule that modulates LPS-induced cytokine secretion by macrophages. J. Leukoc. Biol. *88*, 687–697. https://doi.org/10.1189/jlb.1109756.

45. Cannons, J.L., Qi, H., Lu, K.T., Dutta, M., Gomez-Rodriguez, J., Cheng, J., Wakeland, E.K., Germain, R.N., and Schwartzberg, P.L. (2010). Optimal germinal center responses require a multistage T cell:B cell adhesion process involving integrins, SLAM-associated protein, and CD84. Immunity *32*, 253–265. https://doi.org/10.1016/j.immuni.2010.01.010.

46. Alshetaiwi, H., Pervolarakis, N., McIntyre, L.L., Ma, D., Nguyen, Q., Rath, J.A., Nee, K., Hernandez, G., Evans, K., Torosian, L., et al. (2020). Defining the emergence of myeloid-derived suppressor cells in breast cancer using single-cell transcriptomics. Sci. Immunol. *5*, eaay6017. https://doi.org/10.1126/sciimmunol.aay6017.

47. Lewinsky, H., Gunes, E.G., David, K., Radomir, L., Kramer, M.P., Pellegrino, B., Perpinial, M., Chen, J., He, T.F., Mansour, A.G., et al. (2021). CD84 is a regulator of the immunosuppressive microenvironment in multiple myeloma. JCI Insight *6*, e141683. https://doi.org/10.1172/jci.insight.141683.

48. Pettinella, F., Mariotti, B., Lattanzi, C., Bruderek, K., Donini, M., Costa, S., Marini, O., Iannoto, G., Gasperini, S., Caveggion, E., et al. (2024). Surface CD52, CD84, and PTGER2 mark mature PMN-MDSCs from cancer patients and G-CSF-treated donors. Cell Rep. Med. *5*, 101380. https://doi.org/10.1016/j.xcrm.2023.101380.

49. Xie, X., Shi, Q., Wu, P., Zhang, X., Kambara, H., Su, J., Yu, H., Park, S.Y., Guo, R., Ren, Q., et al. (2020). Single-cell transcriptome profiling reveals neutrophil heterogeneity in homeostasis and infection. Nat. Immunol. *21*, 1119–1133. https://doi.org/10.1038/s41590-020-0736-z.

50. Gullotta, G.S., De Feo, D., Friebel, E., Semerano, A., Scotti, G.M., Bergamaschi, A., Butti, E., Brambilla, E., Genchi, A., Capotondo, A., et al. (2023). Age-induced alterations of granulopoiesis generate atypical neutrophils that aggravate stroke pathology. Nat. Immunol. *24*, 925–940. https://doi.org/10.1038/s41590-023-01505-1.

51. Gebhardt, C., Németh, J., Angel, P., and Hess, J. (2006). S100A8 and S100A9 in inflammation and cancer. Biochem. Pharmacol. *72*, 1622–1631. https://doi.org/10.1016/j.bcp.2006.05.017.

52. Adrover, J.M., Del Fresno, C., Crainiciuc, G., Cuartero, M.I., Casanova-Acebes, M., Weiss, L.A., Huerga-Encabo, H., Silvestre-Roig, C., Rossaint, J., Cossío, I., et al. (2019). A Neutrophil Timer Coordinates Immune Defense and Vascular Protection. Immunity *50*, 390–402.e10. https://doi.org/10.1016/j.immuni.2019.01.002.

53. Chang, C.W., Cheng, N., Bai, Y., Skidgel, R.A., and Du, X. (2021). Galpha(13) Mediates Transendothelial Migration of Neutrophils by Promoting Integrin-Dependent Motility without Affecting Directionality. J. Immunol. *207*, 3038–3049. https://doi.org/10.4049/jimmunol.2001385.

54. Lighvani, S., Baik, N., Diggs, J.E., Khaldoyanidi, S., Parmer, R.J., and Miles, L.A. (2011). Regulation of macrophage migration by a novel plasminogen receptor Plg-R KT. Blood *118*, 5622–5630. https://doi.org/10.1182/blood-2011-03-344242.

55. Lu, H., Kuang, Y.H., Su, J., Chang, J., Wu, L.S., Kanekura, T., Li, D., Chen, M.L., and Chen, X. (2010). CD147 is highly expressed on peripheral blood neutrophils from patients with psoriasis and induces neutrophil chemotaxis. J. Dermatol. *37*, 1053–1056. https://doi.org/10.1111/j.1346-8138.2010.00935.x.

56. Michel, L., Grasmuck, C., Charabati, M., Lécuyer, M.A., Zandee, S., Dhaeze, T., Alvarez, J.I., Li, R., Larouche, S., Bourbonnière, L., et al. (2019). Activated leukocyte cell adhesion molecule regulates B lymphocyte migration across central nervous system barriers. Sci. Transl. Med. *11*, eaaw0475. https://doi.org/10.1126/scitranslmed.aaw0475.

57. Ochsner, S.A., Abraham, D., Martin, K., Ding, W., McOwiti, A., Kankanamge, W., Wang, Z., Andreano, K., Hamilton, R.A., Chen, Y., et al. (2019). The Signaling Pathways Project, an integrated 'omics knowledgebase for mammalian cellular signaling pathways. Sci. Data *6*, 252. https://doi.org/10.1038/s41597-019-0193-4.

58. Bolis, M., Bossi, D., Vallerga, A., Ceserani, V., Cavalli, M., Impellizzieri, D., Di Rito, L., Zoni, E., Mosole, S., Elia, A.R., et al. (2021). Dynamic prostate cancer transcriptome analysis delineates the trajectory to disease progression. Nat. Commun. *12*, 7033. https://doi.org/10.1038/s41467-021-26840-5.

59. Veglia, F., Hashimoto, A., Dweep, H., Sanseviero, E., De Leo, A., Tcyganov, E., Kossenkov, A., Mulligan, C., Nam, B., Masters, G., et al. (2021). Analysis of classical neutrophils and polymorphonuclear myeloid-derived suppressor cells in cancer patients and tumor-bearing mice. J. Exp. Med. *218*, e20201803. https://doi.org/10.1084/jem.20201803.

60. Koizume, S., Jin, M.S., Miyagi, E., Hirahara, F., Nakamura, Y., Piao, J.H., Asai, A., Yoshida, A., Tsuchiya, E., Ruf, W., and Miyagi, Y. (2006). Activation of cancer cell migration and invasion by ectopic synthesis of coagulation factor VII. Cancer Res. *66*, 9453–9460. https://doi.org/10.1158/0008-5472.CAN-06-1803.

61. Deng, X., Feng, Z., Zhu, L., Chen, N., Deng, Y., Li, Y., Li, R., Wang, L., Luo, M., and Wu, J. (2020). Platelet-Derived Factor V Is an Important Determinant of the Metastatic Potential of Circulating Tumor Cells. Front. Oncol. *10*, 558306. https://doi.org/10.3389/fonc.2020.558306.

62. Nierodzik, M.L., and Karpatkin, S. (2006). Thrombin induces tumor growth, metastasis, and angiogenesis: Evidence for a thrombin-regulated dormant tumor phenotype. Cancer Cell *10*, 355–362. https://doi.org/10.1016/j.ccr.2006.10.002.

63. de Bono, J.S., Harris, J.R., Burm, S.M., Vanderstichele, A., Houtkamp, M.A., Aarass, S., Riisnaes, R., Figueiredo, I., Nava Rodrigues, D., Christova, R., et al. (2023). Systematic study of tissue factor expression in solid tumors. Cancer Rep. *6*, e1699. https://doi.org/10.1002/cnr2.1699.

64. Hettiarachchi, R.J., Smorenburg, S.M., Ginsberg, J., Levine, M., Prins, M.H., and Büller, H.R. (1999). Do heparins do more than just treat thrombosis? The influence of heparins on cancer spread. Thromb. Haemost. *82*, 947–952.

65. Prandoni, P., Lensing, A.W., Büller, H.R., Carta, M., Cogo, A., Vigo, M., Casara, D., Ruol, A., and ten Cate, J.W. (1992). Comparison of subcutaneous low-molecular-weight heparin with intravenous standard heparin in proximal deep-vein thrombosis. Lancet *339*, 441–445. https://doi.org/10.1016/0140-6736(92)91054-c.

66. Klerk, C.P.W., Smorenburg, S.M., Otten, H.M., Lensing, A.W.A., Prins, M.H., Piovella, F., Prandoni, P., Bos, M.M.E.M., Richel, D.J., van Tienhoven, G., and Büller, H.R. (2005). The effect of low molecular weight heparin on survival in patients with advanced malignancy. J. Clin. Oncol. *23*, 2130–2135. https://doi.org/10.1200/JCO.2005.03.134.

67. Schulman, S., and Lindmarker, P. (2000). Incidence of cancer after prophylaxis with warfarin against recurrent venous thromboembolism. Duration of Anticoagulation Trial. N. Engl. J. Med. *342*, 1953–1958. https://doi.org/10.1056/NEJM200006293422604.

68. Kaur, H., Siemens, D.R., Black, A., Robb, S., Barr, S., Graham, C.H., and Othman, M. (2017). Effects of androgen-deprivation therapy on hypercoagulability in prostate cancer patients: A prospective, longitudinal study. Can. Urol. Assoc. J. *11*, 33–38. https://doi.org/10.5489/cuaj.3936.

69. Klil-Drori, A.J., Yin, H., Tagalakis, V., Aprikian, A., and Azoulay, L. (2016). Androgen Deprivation Therapy for Prostate Cancer and the Risk of Venous Thromboembolism. Eur. Urol. *70*, 56–61. https://doi.org/10.1016/j.eururo.2015.06.022.

70. Kapoor, S., Opneja, A., and Nayak, L. (2018). The role of neutrophils in thrombosis. Thromb. Res. *170*, 87–96. https://doi.org/10.1016/j.thromres.2018.08.005.

71. Dean, M.J., Ochoa, J.B., Sanchez-Pino, M.D., Zabaleta, J., Garai, J., Del Valle, L., Wyczechowska, D., Baiamonte, L.B., Philbrook, P., Majumder, R., et al. (2021). Severe COVID-19 Is Characterized by an Impaired Type I Interferon Response and Elevated Levels of Arginase Producing Granulocytic Myeloid Derived Suppressor Cells. Front. Immunol. *12*, 695972. https://doi.org/10.3389/fimmu.2021.695972.

72. Leibowitz-Amit, R., Templeton, A.J., Omlin, A., Pezaro, C., Atenafu, E.G., Keizman, D., Vera-Badillo, F., Seah, J.A., Attard, G., Knox, J.J., et al. (2014). Clinical variables associated with PSA response to abiraterone acetate in patients with metastatic castration-resistant prostate cancer. Ann. Oncol. *25*, 657–662. https://doi.org/10.1093/annonc/mdt581.

73. Schuhmann, M.K., Stoll, G., Bieber, M., Vögtle, T., Hofmann, S., Klaus, V., Kraft, P., Seyhan, M., Kollikowski, A.M., Papp, L., et al. (2020). CD84 Links T Cell and Platelet Activity in Cerebral Thrombo-Inflammation in Acute Stroke. Circ. Res. *127*, 1023–1035. https://doi.org/10.1161/CIRCRESAHA.120.316655.

74. Weiss, L.J., Drayss, M., Mott, K., Droste, M., Just, B., Arold, A.M., Nieswandt, B., Weismann, D., Stegner, D., and Schulze, H. (2022). The homophilic CD84 receptor is upregulated on platelets in COVID-19 and sepsis. Thromb. Res. *220*, 121–124. https://doi.org/10.1016/j.thromres.2022.10.011.

75. Garlapati, V., Molitor, M., Michna, T., Harms, G.S., Finger, S., Jung, R., Lagrange, J., Efentakis, P., Wild, J., Knorr, M., et al. (2023). Targeting myeloid cell coagulation signaling blocks MAP kinase/TGF-beta1 driven fibrotic remodeling in ischemic heart failure. J. Clin. Invest. *133*, e156436. https://doi.org/10.1172/JCI156436.

76. Muller-Calleja, N., Hollerbach, A., Ritter, S., Pedrosa, D.G., Strand, D., Graf, C., Reinhardt, C., Strand, S., Poncelet, P., Griffin, J.H., et al. (2019). Tissue factor pathway inhibitor primes monocytes for antiphospholipid antibody-induced thrombosis. Blood *134*, 1119–1131. https://doi.org/10.1182/blood.2019001530.

77. Zhong, Q., Rüschoff, J.H., Guo, T., Gabrani, M., Schüffler, P.J., Rechsteiner, M., Liu, Y., Fuchs, T.J., Rupp, N.J., Fankhauser, C., et al. (2016). Image-based computational quantification and visualization of genetic alterations and tumour heterogeneity. Sci. Rep. *6*, 24146. https://doi.org/10.1038/srep24146.

78. Welti, J., Sharp, A., Yuan, W., Dolling, D., Nava Rodrigues, D., Figueiredo, I., Gil, V., Neeb, A., Clarke, M., Seed, G., et al. (2018). Targeting Bromodomain and Extra-Terminal (BET) Family Proteins in Castration-Resistant Prostate Cancer (CRPC). Clin. Cancer Res. *24*, 3149–3162. https://doi.org/10.1158/1078-0432.CCR-17-3571.

79. Gil, V., Miranda, S., Riisnaes, R., Gurel, B., D'Ambrosio, M., Vasciaveo, A., Crespo, M., Ferreira, A., Brina, D., Troiani, M., et al. (2021). HER3 Is an Actionable Target in Advanced Prostate Cancer. Cancer Res. *81*, 6207–6218. https://doi.org/10.1158/0008-5472.CAN-21-3360.

80. Fenor de la Maza, M.D., Chandran, K., Rekowski, J., Shui, I.M., Gurel, B., Cross, E., Carreira, S., Yuan, W., Westaby, D., Miranda, S., et al. (2022). Immune Biomarkers in Metastatic Castration-resistant Prostate Cancer. Eur. Urol. Oncol. *5*, 659–667. https://doi.org/10.1016/j.euo.2022.04.004.

81. Guccini, I., Revandkar, A., D'Ambrosio, M., Colucci, M., Pasquini, E., Mosole, S., Troiani, M., Brina, D., Sheibani-Tezerji, R., Elia, A.R., et al. (2021). Senescence Reprogramming by TIMP1 Deficiency Promotes Prostate Cancer Metastasis. Cancer Cell *39*, 68–82.e9. https://doi.org/10.1016/j.ccell.2020.10.012.

82. Chen, Z., Trotman, L.C., Shaffer, D., Lin, H.K., Dotan, Z.A., Niki, M., Koutcher, J.A., Scher, H.I., Ludwig, T., Gerald, W., et al. (2005). Crucial role of p53-dependent cellular senescence in suppression of Pten-deficient tumorigenesis. Nature *436*, 725–730. https://doi.org/10.1038/nature03918.

83. Van Gassen, S., Callebaut, B., Van Helden, M.J., Lambrecht, B.N., Demeester, P., Dhaene, T., and Saeys, Y. (2015). FlowSOM: Using self-organizing maps for visualization and interpretation of cytometry data. Cytometry A. *87*, 636–645. https://doi.org/10.1002/cyto.a.22625.

84. Dobin, A., Davis, C.A., Schlesinger, F., Drenkow, J., Zaleski, C., Jha, S., Batut, P., Chaisson, M., and Gingeras, T.R. (2013). STAR: ultrafast universal RNA-seq aligner. Bioinformatics *29*, 15–21. https://doi.org/10.1093/bioinformatics/bts635.

85. van Dijk, D., Sharma, R., Nainys, J., Yim, K., Kathail, P., Carr, A.J., Burdziak, C., Moon, K.R., Chaffer, C.L., Pattabiraman, D., et al. (2018). Recovering Gene Interactions from Single-Cell Data Using Data Diffusion. Cell *174*, 716–729.e27. https://doi.org/10.1016/j.cell.2018.05.061.

86. Stuart, T., Butler, A., Hoffman, P., Hafemeister, C., Papalexi, E., Mauck, W.M., Hao, Y., Stoeckius, M., Smibert, P., and Satija, R. (2019). Comprehensive Integration of Single-Cell Data. Cell *177*, 1888–1902.e21. https://doi.org/10.1016/j.cell.2019.05.031.

87. Hanzelmann, S., Castelo, R., and Guinney, J. (2013). GSVA: gene set variation analysis for microarray and RNA-seq data. BMC Bioinf. *14*, 7. https://doi.org/10.1186/1471-2105-14-7.

88. Love, M.I., Huber, W., and Anders, S. (2014). Moderated estimation of fold change and dispersion for RNA-seq data with DESeq2. Genome Biol. *15*, 550. https://doi.org/10.1186/s13059-014-0550-8.

89. Durinck, S., Spellman, P.T., Birney, E., and Huber, W. (2009). Mapping identifiers for the integration of genomic datasets with the R/Bioconductor package biomaRt. Nat. Protoc. *4*, 1184–1191. https://doi.org/10.1038/nprot.2009.97.

90. Korotkevich, G., Sukhov, V., Budin, N., Shpak, B., Artyomov, M.N., and Sergushichev, A. (2021). Fast gene set enrichment analysis. Preprint at bioRxiv. https://doi.org/10.1101/060012.

91. Trotman, L.C., Niki, M., Dotan, Z.A., Koutcher, J.A., Di Cristofano, A., Xiao, A., Khoo, A.S., Roy-Burman, P., Greenberg, N.M., Van Dyke, T., et al. (2003). Pten dose dictates cancer progression in the prostate. PLoS Biol. *1*, E59. https://doi.org/10.1371/journal.pbio.0000059.

92. Solito, S., Pinton, L., De Sanctis, F., Ugel, S., Bronte, V., Mandruzzato, S., and Marigo, I. (2019). Methods to Measure MDSC Immune Suppressive Activity In Vitro and In Vivo. Curr. Protoc. Immunol. *124*, e61. https://doi.org/10.1002/cpim.61.

93. Lechner, M.G., Liebertz, D.J., and Epstein, A.L. (2010). Characterization of cytokine-induced myeloid-derived suppressor cells from normal human peripheral blood mononuclear cells. J. Immunol. *185*, 2273–2284. https://doi.org/10.4049/jimmunol.1000901.

94. Drost, J., Karthaus, W.R., Gao, D., Driehuis, E., Sawyers, C.L., Chen, Y., and Clevers, H. (2016). Organoid culture systems for prostate epithelial and cancer tissue. Nat. Protoc. *11*, 347–358. https://doi.org/10.1038/nprot.2016.006.

95. Bergum, P.W., Cruikshank, A., Maki, S.L., Kelly, C.R., Ruf, W., and Vlasuk, G.P. (2001). Role of zymogen and activated factor X as scaffolds for the inhibition of the blood coagulation factor VIIa-tissue factor complex by recombinant nematode anticoagulant protein c2. J. Biol. Chem. *276*, 10063–10071. https://doi.org/10.1074/jbc.M009116200.

96. Binsky-Ehrenreich, I., Marom, A., Sobotta, M.C., Shvidel, L., Berrebi, A., Hazan-Halevy, I., Kay, S., Aloshin, A., Sagi, I., Goldenberg, D.M., et al. (2014). CD84 is a survival receptor for CLL cells. Oncogene *33*, 1006–1016. https://doi.org/10.1038/onc.2013.31.

97. Marom, A., Barak, A.F., Kramer, M.P., Lewinsky, H., Binsky-Ehrenreich, I., Cohen, S., Tsitsou-Kampeli, A., Kalchenko, V., Kuznetsov, Y., Mirkin, V., et al. (2017). CD84 mediates CLL-microenvironment interactions. Oncogene *36*, 628–638. https://doi.org/10.1038/onc.2016.238.

98. Hothorn, T., and Lausen, B. (2003). On the exact distribution of maximally selected rank statistics. Comput. Stat. Data An. *43*, 121–137.

99. Lausen, B., Hothorn, T., Bretz, F., and Schumacher, M. (2004). Assessment of optimal selected prognostic factors. Biometrical J. *46*, 364–374. https://doi.org/10.1002/bimj.200310030.

100. Ohnishi, S.T., and Devlin, T.M. (1979). Calcium ionophore activity of a prostaglandin B1 derivative (PGBx). Biochem. Biophys. Res. Commun. *89*, 240–245. https://doi.org/10.1016/0006-291x(79)90969-0.

101. Brummelman, J., Haftmann, C., Núñez, N.G., Alvisi, G., Mazza, E.M.C., Becher, B., and Lugli, E. (2019). Development, application and computational analysis of high-dimensional fluorescent antibody panels for single-cell flow cytometry. Nat. Protoc. *14*, 1946–1969. https://doi.org/10.1038/s41596-019-0166-2.

102. Samusik, N., Good, Z., Spitzer, M.H., Davis, K.L., and Nolan, G.P. (2016). Automated mapping of phenotype space with single-cell data. Nat. Methods *13*, 493–496. https://doi.org/10.1038/nmeth.3863.

103. Pernigoni, N., Zagato, E., Calcinotto, A., Troiani, M., Mestre, R.P., Calì, B., Attanasio, G., Troisi, J., Minini, M., Mosole, S., et al. (2021). Commensal bacteria promote endocrine resistance in prostate cancer through androgen biosynthesis. Science *374*, 216–224. https://doi.org/10.1126/science.abf8403.

STAR★METHODS

KEY RESOURCES TABLE

REAGENT or RESOURCE	SOURCE	IDENTIFIER
Antibodies		
Anti-IL-23 monoclonal antibody clone (G23-8)	eBioscience	Cat#16-7232-85; RRID: AB_469241
Rat IgG1 kappa Isotype Control	eBioscience	Cat#16-4301-81; RRID: AB_470153
CD84/SLAMF5 Antibody (152-1D5)	Novus Biologicals	Cat#NBP2-44345
Mouse IgG1 Isotype Control (11711)	Novus Biologicals	Cat#MAB002; RRID: AB_357344
anti-Ki67 Clone SP6	Histocom	Cat#MAD-000310QD-7
Cleaved Caspase-3 (Asp175) Antibody	Cell signaling Technology	Cat#9661; RRID: AB_2341188
Anti-CDKN2A/p16INK4a antibody [EPR20418]	Abcam	Cat# ab211542; RRID: AB_2891084
Anti-PAR2 antibody [EPR13675]	Abcam	Cat# ab180953
Factor X antibody	Genetex	Cat# GTX110300; RRID: AB_1950240
CD15/SSEA1 (MC480) Mouse mAb	Cell signaling Technology	Cat#4744; RRID: AB_1264258
Anti-FX (f21-4.2)-488	Muller-Calleja et al.[76] Ruf Lab	
Anti-Factor VII antibody	Abcam	Cat#ab97614; RRID: AB_10680440
Anti-PAR-1, clone ATAP2 Antibody	Sigma-Aldrich	Cat#MABF244
Tissue Factor/CD142 (E2L3B) Rabbit mAb	Cell signaling Technology	Cat# 44861; RRID: AB_3076292
Phospho-p44/42 MAPK (Erk1/2) (Thr202/Tyr204) Rabbit Antibody	Cell signaling Technology	Cat#9101; RRID: AB_331646
p44/42 MAPK (Erk1/2) Rabbit Antibody	Cell signaling Technology	Cat#9102; RRID: AB_330744
Phospho-Src Family (Tyr416) (D49G4) Rabbit mAb	Cell signaling Technology	Cat#6943; RRID: AB_10013641
Src (32G6) Rabbit mAb	Cell signaling Technology	Cat#2123; RRID: AB_2106047
IRF-8 (D20D8) Rabbit mAb	Cell signaling Technology	Cat#5628; RRID: AB_10828231
Anti-C/EBP epsilon antibody [N1C3]	Genetex	Cat#GTX109155; RRID: AB_10630221
α-Tubulin (DM1A) Mouse mAb	Cell signaling Technology	Cat#3873; RRID: AB_1904178
HSP90 (C45G5) Rabbit mAb	Cell signaling Technology	Cat#4877; RRID: AB_2233307
Purified Rat Anti-Mouse CD16/CD32 (Mouse BD Fc Block™)	BD Bioscience	Cat#553141; RRID: AB_394656
anti-Epcam-FITC (clone G8.8)	Thermo Fisher	Cat#11-5791-82; RRID:11151709
anti-CD45-bv605 (clone 30-F11)	Biolegend	Cat#103140; RRID: AB_2562342
anti-CD11b-bv421 (clone M1/70)	Biolegend	Cat#101236; RRID: AB_11203704
and anti-Gr1-APC (clone RB6-8C5)	Biolegend	Cat#108412; RRID: AB_313377
BUV805 Rat Anti-Mouse CD45 Clone 30-F11	BD Bioscience	Cat#748370; RRID: AB_2872789
PE/Cyanine7 anti-mouse CD3 Antibody (clone17A2)	Biolegend	Cat#100220; RRID: AB_1732057
BUV496 Rat Anti-Mouse CD8a (clone 53-6.7)	BD Bioscience	Cat#750024; RRID: AB_2874242
BD OptiBuild™ BUV395 Rat Anti-Mouse CD4 (clone RM4.5)	BD Bioscience	Cat#740208; RRID: AB_2734761
BD OptiBuild™ BUV563 Rat Anti-Mouse CD19 (1D3)	BD Bioscience	Cat#749028; RRID: AB_2873425
BD Pharmingen™ PE-Cy™5 Rat Anti-Mouse CD45R/B220 (RA3-6B2)	BD Bioscience	Cat#561879; RRID: AB_10898014
BD OptiBuild™ BUV615 Mouse Anti-Mouse NK-1.1 (clone PK136)	BD Bioscience	Cat#751111; RRID: AB_2875140
BD OptiBuild™ BV650 Hamster Anti-Mouse CD49b (HMα2)	BD Bioscience	Cat#740496; RRID: AB_2740219
Cd11b Rat anti Mouse, APC Cy7, (clone M1/70)	BD Bioscience	Cat#561039; RRID: AB_2033993
BD OptiBuild™ BUV737 Rat Anti-Mouse Ly-6G, (clone 1A8)	BD Bioscience	Cat#741813; RRID: AB_2871151
Anti-Ly-6C Rat Monoclonal Antibody (Brilliant Violet® 711) (clone HK1.4)	Biolegend	Cat#128037; $RRID: AB_2562630
IL-23 p19 Monoclonal Antibody, PerCP-eFluor 710, (clonefc23cpg)	eBioscience	Cat# 46-7023-80; RRID: AB_2573824

(*Continued on next page*)

Continued

REAGENT or RESOURCE	SOURCE	IDENTIFIER
R718 Rat Anti-Mouse CD182 (CXCR2) (clone V48-2310)	BD Bioscience	Cat#752139; RRID: AB_2917248
F4/80 Rat anti Mouse, BV480 (clone T45-2342)	BD Bioscience	Cat#565635; RRID: AB_2739313
BD Horizon™ PE-CF594 Rat Anti-Mouse CD103 (clone M290)	BD Bioscience	Cat#565849; RRID: AB_2739377
PE anti-mouse CD84 Antibody (clone mCD84.7)	Biolegend	Cat#122805; RRID: AB_2074757
Brilliant Violet 650™ anti-mouse CD11c Antibody (clone N418)	Biolegend	Cat#117339; RRID: AB_2562414
BD OptiBuild™ BV786 Rat Anti-Mouse I-A/I-E (cloneM5/114.15.2)	BD Bioscience	Cat#742894; RRID: AB_2734759
Brilliant Violet 421 anti-CD3e (clone 145-2c11)	Biolegend	Cat#100341; RRID: AB_2562556
PerCP/Cyanine5.5anti-CD8a (clone 53-6.7)	Biolegend	Cat#100734; RRID: AB_2075238
PE anti-CD4 (clone GK1.5)	Biolegend	Cat#100408; RRID: AB_312693
Human BD Fc Block™(Clone Fc1-RUO)	BD Bioscience	Cat#564220; RRID: AB_2869554
Brilliant Violet 650 anti-CD3 (clone UCHT1)	Biolegend	Cat#300476
PE/Cyanine7 anti-human CD8 Antibody (clone SK1)	Biolegend	Cat#344711; RRID: AB_2044007
APC anti-human CD4 Antibody (clone SK3)	Biolegend	Cat#344613; RRID: AB_2028485
Brilliant Violet 605™ anti-human CD45 Antibody (clone HI30)	Biolegend	Cat#304041; RRID: AB_2562105
CD33 Monoclonal Antibody (WM-53), APC	eBioscience	Cat#17-0338-41; RRID: AB_10667747
Alexa Fluor® 700 anti-human CD14 Antibody(clone 63D3)	Biolegend	Cat#367114; RRID: AB_2566716
PE/Cyanine7 anti-human CD15 (SSEA-1) Antibody (clone HI98)	Biolegend	Cat#301924; RRID: AB_2783155
PE anti-human CD84 Antibody (clone CD84.1.21)	Biolegend	Cat#326008; RRID: AB_2229003
Goat anti-Rabbit IgG (H&L) - Alexa Fluor™ 647	Thermo Fisher	Cat#A-21244; RRID: AB_2535812
Donkey anti-Rabbit IgG (H&L) - Alexa Fluor™ 488	Thermo Fisher	Cat#A-21206; RRID: AB_2535792
Alexa Fluor® 594 anti-mouse/human CD11b Antibody (clone M1/70)	Biolegend,	cat#101254; RRID: AB_2563231
Biological samples		
Human prostate formalin-fixed paraffin-embedded (FFPE) samples	University of Padova & University Hospital Zurich (USZ)[2]	reference no. CESC 5480/AO/22
Human prostate biopsies	Urology Clinic of the University of Padova, Zhong et al. (2016)[77]	reference no. CESC 5170/AO/21
Blood from PCa patients	Urology Clinic of the University of Padova	reference no. CESC 5170/AO/21
Plasma from PCa patients and patient-derived organoids	de Bono Lab[3,4]	reference no. REC 04/Q0801/60
Buffy coats from healthy donors	Swiss Blood Donation Center of Basel and Lugano, Welti et al. (2018),[78] Gil et al. (2021)[79]	reference no. A000197/2
Chemicals, peptides, and recombinant proteins		
Matrigel	Corning	
ACK lysing buffer	Gibco	Cat#A1049201
Recombinant Murine GM-CSF	Peprotech	Cat#315-03
Recombinant Murine IL-6	Peprotech	Cat# 216-16
Recombinant Human GM-CSF	Peprotech	Cat#300-03
Recombinant Human IL-6	Peprotech	Cat#200-06
Ficoll-Hypaque	Sigma-Aldrich	Cat#GE17-1440-03
CD33 MicroBeads, human	Miltenyi Biotec	Cat#130-045-501
Charcoal-stripped FBS	Gibco	Cat#12676029
Recombinant Mouse Coagulation Factor Xa	R&D Systems	Cat#6724-SE-010

(*Continued on next page*)

Continued

REAGENT or RESOURCE	SOURCE	IDENTIFIER
Recombinant Human Coagulation Factor Xa	R&D Systems	Cat#1063-SE-010
Recombinant Mouse IL-23	R&D Systems	Cat#1887-ML
Recombinant Human IL-23	R&D Systems	Cat#1290-IL
Recombinant Human CD84	R&D Systems	Cat#1855-CD-050
CFSE	Thermo Scientific	Cat# C34554
Dynabeads™ Mouse T-Activator CD3/CD28 for T-Cell Expansion and Activation	Thermo Scientific	Cat#11452D
Dynabeads™ Human T-Activator CD3/CD28 for T Cell Expansion and Activation	Thermo Scientific	Cat#11131D
NapC2	ARCA biopharma	
Factor VII	NovoNordisk	
Rivaroxaban	Selleckchem	Cat#S3002
AZ3451	MedChem Express	Cat#HY-112558
ENMD-1068	MedChem Express	Cat#HY-124748A
Go6983	MedChem Express	Cat# HY-13689
Pertussis Toxin	Sigma-Aldrich	Cat# P7208
Enzalutamide	APExBio	Cat# MDV3100
AZD5069	AstraZeneca	
Dalteparin (LMWH)	Pfizer	
Rnase Inhibitor Murine	New England Biolabs	Cat# M0314L
FVS BD Horizon™ Fixable Viability Stain 440UV for viability	BD Biosciences	Cat# 566332
Critical commercial assays		
Human Coagulation Factor X ELISA Kit	Novus Biologicals	Cat# NBP2-60625
Chromium Single Cell 3´ GEM, Library & Gel Bead Kit v3	10x Genomics	Cat# PN-1000075
RNAscope Multiplex Fluorescent Reagent Kit v2	ACD Bio	Cat#323110
RNAscope H2O2 and protease reagents	ACD Bio	Cat#322381
RNAscope Target retrieval reagent	ACD Bio	Cat#322000
RNAscope Probe- Hs FX-C2	ACD Bio	Cat#1333641-C2
TSA Vivid 650 fluorophore	ACD Bio	Cat#323273
RNAscope Multiplex FL v2 DAPI	ACD Bio	Cat#323110
NEBNext® Ultra™ II Directional RNA Library Prep with Sample Purification Beads	New England BioLabs Inc.	Cat#E7765L
NEBNext UltraExpress™ RNA Library Prep Kit	New England BioLabs Inc.	Cat#E3330L
NEBNext® Poly(A) mRNA Magnetic Isolation Module for cDNA synthesis	New England BioLabs Inc.	Cat#E7490
Deposited data		
SU2C cohort RNA-seq and clinical data	Robinson et al.[38]	https://doi.org/10.1016/j.cell.2015.05.001
RMH cohort RNA-seq and clinical data	Fenor de la Maza et al.[80]	https://doi.org/10.1016/j.euo.2022.04.004
Bulk-RNAseq human prostate cancer	Bolis et al.[58]	https://www.pcaprofiler.com.
scRNA-seq HS *Pten*$^{pc/-}$ mouse prostate (10-week)	Guccini et al.[81]	ArrayExpress: E-MTAB-9578
scRNA of human PCa patients	Hirz et al.[32]	GEO: GSE181294
Bulk RNA-seq of wild-type and *Pten*$^{pc/-}$ mouse prostate	Brina et al.[8]	ArrayExpress: E-MTAB-9624
scRNA of the immune infiltrate of TRAMP-C1 allografts	This paper	GEO: GSE272999
scRNA of HS (24-week) and CR *Pten*$^{pc/-}$ mouse prostate	This paper	GEO: GSE272965
Bulk RNA-seq of IVD-hMDSCs upon CD84 ligation	This paper	GEO: GSE272966
Bulk RNA-seq of CRPC *Pten*$^{pc-/-}$ mice reconstituted with either *F10*$^{fl/fl}$ or *F10*$^{fl/fl}$*; LysM-Cre*$^{+}$ mice	This paper	GEO: GSE272967
Experimental models: Cell lines		
TRAMPC1	ATCC	Cat#CRL-2730; RRID: CVCL_3614
LNCaP clone FGC	ATCC	Cat#CRL-1740; RRID: CVCL_1379

(*Continued on next page*)

Continued

REAGENT or RESOURCE	SOURCE	IDENTIFIER
RapidCaP	Cho et al.[28] Trotman laboratory (Cold Spring Harbor Laboratory, Cancer Center)	
RM-1	ATCC	Cat#CRL-3310 RRID: CVCL_B459
LapC4	Theurillat laboratory	RRID:CVCL_4744
DU 145	ATCC	Cat# HTB-81
22Rv1	ATCC	Cat#CRL-2505; RRID: CVCL_1045
PC3	ATCC	Cat#CRL-1435; RRID: CVCL_0035
LNCAP-Abl	Theurillat laboratory	
VCAP	Theurillat laboratory	Cat# CRL-2876
RWPE-1	ATCC	Cat#CRL-11609; RRID: CVCL_3791
BPH-1	Sigma-Aldrich	Cat. # SCC256
HEK-293T (human embryonic kidneys)	ATCC	Cat#CRL-3216; RRID: CVCL_0063
Experimental models: Organisms/strains		
Pten$^{pc-/-}$	Chen et al.[82]	
F10$^{fl/fl}$*; LysM-Cre*	Graf et al.[17]	
Mouse- C57BL/6N	Charles River	RRID:MGI:2159965
Mouse- NOD-Rag2tm1-IL2rgtm1 (NRG)	Charles River	RRID:IMSR_RJ:NRG
Oligonucleotides		
Primer:hF10 For 5' –AGATGGCGACCAGTGTGAGA– 3'	Sigma-Aldrich	
Primer:hF10 Rev 5'–GTGCAGGTGTATTCCCCGAG– 3'	Sigma-Aldrich	
Primer:hCD84 For 5' –ACCGCAGCTAGGAATAATG– 3'	Sigma-Aldrich	
Primer:hCD84 Rev 5'–CGGAATAAACTGTGTTCACTG– 3'	Sigma-Aldrich	
Primer:mF10 For 5'–TTCCGGATGAACGTGGCCCCT–3'	Sigma-Aldrich	
Primer:mF10 Rev 5'–ATGCGTGCGTCCAAAACCGCT–3'	Sigma-Aldrich	
Primer:mCd84 For 5'-ATATAGCTGGAGTCCCTTTGGAG– 3'	Sigma-Aldrich	
Primer:mCd84 Rev 5'AAAGAGCACGGCCAATCCTC– 3'	Sigma-Aldrich	
Primer:r18S For 5'–ACCGCAGCTAGGAATAATG –3'	Sigma-Aldrich	
Primer:r18S Rev 5'–GCCTCAGTTCCGAAAACCA–3'	Sigma-Aldrich	
Recombinant DNA		
pLV[shRNA]-Puro-U6>m*F3*[shRNA#1]	VectorBuilder	Cat#VB220216-1140ycj
pLV[shRNA]-Puro-U6>Scramble_shRNA#1	VectorBuilder	Cat#VB010000-0005mme
Software and algorithms		
Leica Application Suite X (LAS X)	Leica	RRID:SCR_013673
Graphpad Prism v.9	GraphPad by Dotmatics	RRID: SCR_002798
BD FACSDiva software version 8.0.1	BD	RRID: SCR_001456
FlowJo_10.8.1	BD	RRID: SCR_008520
UMAP plugin FlowJo	BD, https://arxiv.org/abs/1802.03426	https://www.flowjo.com/exchange/#/plugin/profile?id=6, RRID:SCR_018217
FlowSOM plugin FlowJo	BD, Van Gassen et al.[83]	https://www.flowjo.com/exchange/#/plugin/profile?id=7, RRID:SCR_016899
CellRanger (version 3.1.0)	N/A	
R (v.4.3.2)	R CRAN	https://www.r-project.org/
STAR (v.2.7.10a)	Dobin et al.[84]	https://github.com/alexdobin/STAR
RMagic	van Dijk et al.[85]	https://github.com/cran/Rmagic
Seurat	Stuart et al.[86]	https://cran.r-project.org/web/packages/Seurat/index.html
ggplot2 (v.3.4.0)	N/A	https://github.com/tidyverse/ggplot2, RRID:SCR_014601

(*Continued on next page*)

Continued

REAGENT or RESOURCE	SOURCE	IDENTIFIER
Survival	R CRAN	https://cran.r-project.org/web/packages/survival
fgsea	N/A	https://github.com/ctlab/fgsea
Pheatmap	N/A	RRID:SCR_016418
GSVA (v.1.50.5)	Hanzelmann et al.[87]	https://github.com/rcastelo/GSVA
DESeq2	Love et al.[88]	https://github.com/mikelove/DESeq2
biomaRt package	Durinck et al,[89]	https://github.com/grimbough/biomaRt
Fgsea package	Korotkevich et al.[90]	https://github.com/ctlab/fgsea
IncuCyte imaging system	Essen BioScience	RRID:SCR_019874
Aperio ImageScope	Leica (V 12.3.2.8013)	https://www.leicabiosystems.com/digital-pathology/manage/aperio-imagescope/, RRID: SCR_014311
Leica Application Suite X (LAS X)	Leica	RRID:SCR_013673
FIJI Image J	https://imagej.net/software/fiji/downloads	RRID:SCR_002285
Adobe Illustrator		RRID:SCR_010279

EXPERIMENTAL MODEL AND STUDY PARTICIPANT DETAILS

Cell lines

TRAMP-C1 (ATCC® CRL-2730™), RM-1 (ATCC® CRL-3310™), LNCaP (ATCC® CRL-1740™), PC-3 (ATCC® CRL-1435), 22Rv1 (ATCC® CRL-2505™), DU145 (ATCC® HTB-81™) PCa epithelial cells were purchased from ATCC. RapidCap were obtained from Lloyd C Trotman laboratory.[28] VCaP, LapC4 and LNCaP-Abl were provided by Jean-Philippe Theurillat laboratory. TRAMP-C1, RM-1, RapidCap, VCaP, HEK-293T (ATCC® CRL-3216) were cultured in DMEM (Thermo Fisher Scientific), 10% heat-inactivated FBS (Capricorn Scientific GmbH), 100 U/ml penicillin, 0.1 mg/ml streptomycin (Sigma-Aldrich).

LNCaP, PC-3, 22Rv1, DU145, were cultured in RPMI 1640 (Thermo Fisher Scientific), 10% heat-inactivated FBS (Capricorn Scientific GmbH), 100 U/ml penicillin, 0.1 mg/ml streptomycin (Sigma-Aldrich). For LNCAP-Abl charcoal-stripped FBS medium was used (Gibco).

BPH-1 cells were maintained in RPMI 1640 medium supplemented with 20 ng/ml of testosterone, 5 μg/ml of transferrin, 5 ng/ml of sodium selenite, 5 μg/ml of insulin, 20% fetal bovine serum, and 100 U/ml penicillin, 0.1 mg/ml streptomycin (Sigma-Aldrich). RWPE-1 human normal prostate epithelial cells were cultured according to the manufacturer's instructions in Keratinocyte Serum-Free Medium (K-SFM) Medium (17005-042, GIBCO) supplemented with 0.05 mg/ml Bovine Pituitary Extract (BPE), 5 ng/ml human recombinant Epidermal Growth Factor (EGF), 0.1 mg/ml streptomycin (Sigma-Aldrich).

All the cell lines were regularly tested for Mycoplasma by using (MycoAlert Mycoplasma Detection kit, Lonza, Cat. LT07-218).

For *in vitro* experiments, TRAMP-C1, RM-1, RapidCaP, and LNCaP cells were starved in charcoal-stripped FBS medium plus Enzalutamide (APExBio, cat. MDV3100) 10 μM for 72 hours and then kept in full androgen-deprivation medium for all the duration of the experiment (FAD; either DMEM or RMPI 1640 containing 10% heat-inactivated charcoal-stripped FBS plus ENZA 10 μM).

Mouse models

Mice were maintained under specific pathogen-free conditions in the BIOS+ Animal Facility and experiments were approved by the local ethical committee (TI 32/2018 and TI34303). For ethical reasons the minimum number of animals necessary to achieve the scientific objectives was used. Prostate specific *Pten*$^{-/-}$ (*Pten*$^{pc-/-}$) mice were generated and genotyped as previously described.[4,91,82]

Female *Pten*$^{loxP/loxP}$ mice were crossed with male *PB-Cre4* transgenic mice and genotyped for Cre using following primers: primer 1 (5'-AAAAGTTCCCCTGCTGATGATTTGT-3') and primer 2 (5'-TGTTTTTGACCAATTAAAGTAGGCTGTG-3') for *Pten*$^{loxP/loxP}$; primer1 (5' TGATGGACATGTTCAGGGATC 3') and primer2 (5'CAGCCACCAGCTTGCATGA 3') for *Probasin-CRE*.

F10$^{fl/fl}$*; LysM-Cre* mice were obtained from Wolfram Ruf laboratory.[17] Surgical castration was performed on 8-week-old *Pten*$^{pc-/-}$ mice and, for allografts, when tumors were approximately 100 mm^3, under anesthesia with isoflurane as previously described.[4]

For allografts experiments, 5-week-old male C57BL6/N, C57BL6/J and NRG mice were purchased from Charles River (Calco, Italy) and acclimatized for two weeks before experimentation. TRAMP-C1 cells (2.5x10^6) were injected in 8-week-old male C57BL6/N mice.

RM-1 cells (0.2 x10^6) were injected in 8-week-old male C57BL6/J mice. LNCaP cells (2.5x10^6) were subcutaneously injected in matrigel (Corning®, Cat.356231) of male 8-week-old NRG mice. All the allografts were performed by subcutaneous injection in the right flank of the mice. Tumor volume was calculated as $4/3\pi$ (R1 × R2 ×R3), where R1 and R2 are the longitudinal and lateral radii and R3 is the thickness of the tumor that protrudes from the surface of normal skin.[4]

Human samples

Blood from healthy donors was obtained from the Swiss Blood Donation Center of Basel and Lugano and used in compliance with the Federal Office of Public Health (authorization no. A000197/2 to Prof. Federica Sallusto, IRB, Bellinzona, Switzerland).

Patient blood and tumor samples were collected at the Urology Clinic of the University of Padova. Patients had at diagnosis a median age of 64 years. Tissue samples were collected from prostatic needle biopsies, transurethral resections of the prostate or prostatectomies. All patients had given written informed consent and were enrolled in institutional protocols approved by the Padova Province Clinical Experimentation Ethics Committee (reference no. CESC 5170/AO/21).

CRPC plasma and organoids from patient-derived-xenografts[78,79] were obtained from patients identified from a population of men with CRPC treated at the Royal Marsden NHS Foundation Trust. All patients had given written informed consent and were enrolled in institutional protocols approved by the Royal Marsden Hospital (London, UK) ethics review committee (reference no. 04/Q0801/60). Patients did not receive compensation. All tissue blocks were re-sectioned and reviewed by a pathologist who confirmed adequacy of the material.

Human TMA samples were processed and obtained from Universitätsspital Zürich (USZ).[77] Specimens were collected between 1993 and 2007 from the Institute of Surgical Pathology, University Hospital of Zurich, Switzerland. Median follow-up was 132 months.

In vitro-generation of MDSCs and collection of MDSC-CM

Mouse immunosuppressive myeloid cells were differentiated *in vitro* as previously described.[92] Briefly, bone marrow precursors were flushed from the femurs of C57BL/6, *F10*$^{fl/fl}$; *LysM-Cre*$^{+}$ or *F10*$^{fl/fl}$; *LysM-Cre*$^{-}$ mice with RPMI 1640 (Thermo Fisher Scientific). The cell pellet was devoid of red blood cells using ACK lysing buffer (Gibco; A1049201). Then cell suspensions were filtered through 40 μm cell strainers, checked for viability using trypan blue, and resuspended in RPMI 1640 containing 10% heat-inactivated FBS (Capricorn Scientific GmbH), 100 U/ml penicillin, 0.1 mg/ml streptomycin (Sigma-Aldrich). Cells were cultured in the presence of 40 ng/ml mGM-CSF (Peprotech, 315-03) and 40 ng/ml mIL-6 (Peprotech) for 4 days. On day 4, the cells were analyzed by flow cytometry and used for *in vitro* experiments.

Human immunosuppressive myeloid cells were differentiated *in vitro* as previously described.[93] Briefly, human PBMCs were isolated from healthy volunteer donors by venipuncture, followed by differential density gradient separation (Ficoll-Hypaque; Sigma-Aldrich, St. Louis, MO). CD33^{+} myeloid cells were then isolated using anti-CD33 magnetic microbeads and LS column separation (Miltenyi Biotec, Germany) as per manufacturer's instructions. The purity of the isolated cell population was greater than 90% by flow cytometry and the viability of isolated cells was confirmed using trypan blue dye exclusion. Purified CD33^{+} cells were then cultured in RPMI 1640 (Thermo Fisher Scientific) 10% heat-inactivated FBS (Capricorn Scientific GmbH), 100 U/ml penicillin, 0.1 mg/ml streptomycin (Sigma-Aldrich) in the presence of 50 ng/ml hGM-CSF (Peprotech) and 50 ng/ml hIL-6 (Peprotech) for one week. Cytokines were refreshed after 4 days. At day 7, cells were analysed by flow cytometry and used for *in vitro* experiments.

For the preparation of conditioned media, immunosuppressive myeloid cells were resuspended at the density of 0.5 x 10^6 /ml in fresh medium containing 10% heat-inactivated charcoal-stripped FBS (Gibco), 100 U/ml penicillin, 0.1 mg/ml streptomycin (Sigma-Aldrich) and cultured in 6-well plates. Cells were incubated 24 hours at 37°C, 5% CO_2. Then, the conditioned medium (CM) was centrifuged at 500g for 5 min, 2,000 g for 10 min and 4,600 g for 20 min at 4°C to remove dead cells and debris. The medium was then aliquoted in single-use tubes and stored at -80°C.

Cell proliferation assays

PCa cells were kept in full androgen-deprivation medium (FAD) for three days before performing the experiments.[4] Then, mouse TRAMP-C1 and RapidCaP cells were seeded in 96-well plates in fresh FAD medium and treated or not with 100ng/ml recombinant mouse FXa (6724-SE, R&D Systems) or recombinant IL-23 (1887-ML, R&D Systems). Human LNCaP cells kept in FAD were treated or not with 100ng/ml recombinant FXa (6723-SE, R&D Systems) or recombinant human IL-23 (1290-IL, R&D Systems). For experiments with conditioned media, both human and mouse CM was diluted 1:1 in fresh FAD medium. When indicated, Rivaroxaban and AZ3451 were used at the final concentration of 50 μM and 10 μM, respectively. Optimal culture medium (Normal) was used as internal control of proliferation. Images were recorded using a 10× objective and the IncuCyte imaging system (Essen BioScience). The IncuCyte software was used to calculate mean confluence from four non-overlapping bright phase images of each well every 6 hours for at least 3 days.

PDX-O proliferation assay

Tumor tissue from patient-derived xenografts were mechanically dissociated into small pieces in Petri dishes using sterile scalpel blades mixed with sterile PBS and additional ROCK inhibitor Y27632 at 10 μM (S1049, Selleckchem). Samples were filtered through cell strainers 40μm (431750, Corning). Red blood cell lysis was performed using ammonium chloride solution (07850, StemCell Technologies). If a large piece of tissue remained undissociated, cell strainers were used to obtain a pellet for single-cell suspension. Samples were rinsed with cold PBS-containing Y27632, centrifuged at 2000 rpm for 5 minutes and CellTrics® 50μm (Sysmex) was used to generate single-cell suspensions. Cells were embedded at a ratio of 2/1 (matrix:cells) onto Matrigel® (356231, Corning). A standard sterile 24-well plate was pre-warmed at 37°C before use, an aliquot of 50 μl/well was placed in the center of the well; the plate was turned upside down to generate a 'hanging-drop' and immediately incubated at 37°C. Freshly prepared culture medium was overlaid and replenished weekly. PDO cultures were monitored daily and organoid visualized after 3-5 days. PDO culture largely followed the protocol published by Drost et al., 2016 using epithelial prostate niche factors: EGF, Noggin and R-Spondin (Peprotech).[94] Organoid

growth conditions were optimized for each PDX-O model. PDO base media was modified with additional metabolites and growth factors to improve proliferation and viability. Additional factors included: Glutamine (Gibco), Sodium Pyruvate (Sigma), and recombinant human NRG1 (100-03, Peprotech). PDOs were embedded in Matrigel® matrix (356231, Corning) and seeded in replicates in 96-well format optical plates (3904, Corning). Measurements started when organoids developed (baseline, day 0) and proliferation/viability was assessed after 4-days exposure to IVD-hMDSC. Image analysis was performed using Cytation 5 Multimode Reader from Biotek.

In vitro mouse T cell suppression assay

Immunosuppression assays were carried out as previously described.[4,92] Briefly, naive mouse splenocytes were labelled with 5μM CFSE (Molecular Probes) and activated *in vitro* with anti-CD3 and anti-CD28 beads (11452D, Thermo Fischer Scientific) according to the manufacturer's instructions. Either *F10*$^{fl/fl}$*; LysM-Cre*$^{+}$ or *F10*$^{fl/fl}$ BM-MDSCs were added to the culture at different ratios with T cells. After 3 days, cells were stained with Brilliant Violet 421 anti-CD3e (clone 145-2c11); PerCP/Cyanine5.5anti-CD8a (clone 53-6.7); PE anti-CD4 (clone GK1.5) and the proliferation of CFSE-labelled CD8^{+} T cells was was analyezd using the BD LSR Fortessa.

In vitro human T cell suppression assay

Frozen PBMCs from the matched donors were thawed on the same day of the experiments. After 4 hours in culture, PBMCs were labelled with 5μM CFSE (Molecular Probes) and activated *in vitro* with anti-CD3 and anti-CD28 beads (11161D, Thermo Fischer Scientific) according to the manufacturer's instructions.[92] IVD-hMDSCs were added to the culture at different ratios with T cells, in the presence of 30 U/mL recombinant hIL-2 (Peprotech). After 4-5 days, cells were stained with Brilliant Violet 650 anti-CD3 (clone UCHT1); PeCy7 anti-CD8a (clone SK1); APC anti-CD4 (clone SK3) and the proliferation of CFSE-labelled CD8^{+} T cells was analyzed using the FACSymphony™ A5 (BD Biosciences).

Generation of a sh*F3* TRAMP-C1 cells

TRAMP-C1 cell cells were infected with either the human TF-directed shRNA pLV[shRNA]-Puro-U6>mF3[shRNA#1] or pLV[shRNA]-Puro-U6>Scramble_shRNA#1 from VectorBuilder. Briefly, lentiviral particles were produced by transfection of HEK-293T cells using JetPRIME transfection reagents (JetPRIME, Polyplus transfection, 114-07/712-60) according to the manufacturer's instructions. TRAMP-C1 cells were then infected with the filtered lentiviral supernatant suspension obtained from transfected HEK-293T cells. Infected PCa cells were subsequently selected using Puromycin (5 μg/ml).

FXa generation assay

TRAMP-C1 cells were seeded in 12-well plates (1x10^{5}/well) and cultured for three days in a medium containing charcoal-stripped FBS (CS-FBS) for full-androgen deprivation as well as enzalutamide. Medium was replaced with serum free medium for 20 min, followed by one wash with HBSS/Ca^{2+}. FXa generation was measured in the same buffer containing 50 nM FX with or without 2 nM mouse VIIa, and 200 nM of the TF inhibitor nematode anticoagulant protein c2(NAPc2).[75,95] Supernatants were quenched and FXa activity was measured with Spectrozyme FXa in a Spectramax kinetic plate reader.

In vitro FXa-PAR2 stimulation

PCa cells were kept in full androgen-deprivation medium (FAD) for three days, before performing the experiments.[4] Cells were gently detached using a cell scraper, centrifuged and resuspended in fresh FAD medium at the cell density of (1-2x10^{6}/ml). 100ng/ml recombinant mouse FXa (6724-SE, R&D Systems) was used to stimulate TRAMP-C1 cells. Human LNCaP cells were treated or not with 100ng/ml human recombinant FXa (6723-SE, R&D Systems). For experiments with conditioned media, both human and mouse CM was diluted 1:1 in fresh FAD medium. When indicated, cells were pretreated with Rivaroxaban (50 μM, S3002, Selleckchem), AZ3451 (10 μM, HY-112558, MedChem Express), ENMD-1068 (0.5mM, HY-124748A, MedChem Express), Go6983 (10 μM, HY-13689, MedChem Express) and Pertussis Toxin (100ng/ml, P7208, Sigma-Aldrich) for 30 min at 37°C before stimulation with either FXa or CM. Cells stimulation was performed for 30 min at 37°C. Then, samples were washed with ice-cold DPBS and immediately processed for protein extraction.

In vitro CD84 activation

At day 5 of their differentiation, 1 x 10^{6} hIVD-MDSC were exposed with either 2.5 μg/ml of CD84 (Novus Biologicals, Clone 152-1D5) stimulating antibody[47,96,97] or recombinant human CD84 (1855-CD, R&D Systems 10μg/ml). Stimulation was performed in RPMI 1640 (Thermo Fisher Scientific) 10% heat-inactivated FBS (Capricorn Scientific GmbH), 100 U/ml penicillin, 0.1 mg/ml streptomycin (Sigma-Aldrich) in the presence of 50 ng/ml hGM-CSF (Peprotech) and 50 ng/ml hIL-6 (Peprotech) at for 48 hours.

qPCR

CD45^{+} CD11b^{+} Ly6G^{+} myeloid cells were isolated from tumors by FACS sorting and collected in TRIzol™ LS Reagent (Thermo Fischer Scientific, # 10296028). RNA isolation and reverse-transcription were performed using ImProm-II™ Reverse Transcription System (Promega, #A3802) following manufacturer's instructions. qPCR reactions (Promega, #A6002) were performed in duplicates using KAPA SYBR FAST qPCR green (KK4605; Applied Biosystems) and the specific primers reported below. Primer sequences were obtained from PrimerBank (http://pga.mgh.harvard.edu/primerbank/index.html) or Bio-Rad. The human primer sequences

used were as follows[17,97]: *F10 Forward* 5'–AGATGGCGACCAGTGTGAGA–3'; *F10 Reverse* 5'–GTGCAGGTGTATTCCCCGAG–3'; *CD84 Forward* 5'–ACCGCAGCTAGGAATAATG–3'; *CD84 Reverse* 5'–CGGAATAAACTGTGTTCACTG–3'. The mouse primer sequences used were as follows[17,97]: *F10 Forward* 5'–TTCCGGATGAACGTGGCCCCT–3';*F10 Reverse* 5'–ATGCGTGCGTCC AAAACCGCT–3'; *Cd84 Forward* 5'– ATATAGCTGGAGTCCCTTTGGAG– 3'; *Cd84 Reverse* 5'AAAGAGCACGGCCAATCCTC– 3'. Expression levels were normalized to the expression of the housekeeping gene *r18S*, analyzed using the following primers: *r18S Forward* 5'–ACCGCAGCTAGGAATAATG –3'; *r18S Reverse* 5'–GCCTCAGTTCCGAAAACCA–3'.

Western blotting

Tissue and cell lysates were prepared with RIPA buffer (1× PBS, 1% Nonidet P40, 0.5% sodium deoxycholate, 0.1% SDS and protease and phosphatase inhibitor cocktail; Roche). The total protein concentration was measured using a BCA Protein Assay Kit (23225; Pierce). Equal amounts of proteins were separated by SDS–PAGE. Membranes were blocked in 5% BSA in phosphate-buffered saline containing 0.1% Tween-20 (PBST), probed with diluted antibodies, and incubated at 4°C overnight. The following primary antibodies were used: Factor X antibody (Genetex, GTX110300), Anti-Factor VII antibody (Abcam, ab97614); Anti-Par2 antibody (Abcam, ab180953); Anti-Par1 antibody (Sigma-Aldrich, MABF244); Tissue Factor/CD142 (E2L3B) Rabbit mAb (#44861); Phospho-p44/42 MAPK (Erk1/2) (Thr202/Tyr204) Rabbit Antibody (#9101), p44/42 MAPK (Erk1/2) Rabbit Antibody (#9102), Phospho-Src Family (Tyr416) (D49G4) Rabbit mAb (#6943), Src (32G6) Rabbit mAb (#2123), IRF-8 (D20D8) Rabbit mAb (#5628), Anti-C/EBP epsilon antibody [N1C3] (Genetex, GTX109155), α-Tubulin (DM1A) Mouse mAb (#3873), HSP90 (C45G5) Rabbit mAb (#4877), all from Cell Signaling. Membranes were incubated with secondary antibodies that were conjugated to horseradish peroxidase (HRP) (1:5000 dilution, Cell Signaling). The protein bands were visualized using the ECL Western Blotting Substrate (Pierce) and analyzed by ImageJ Software.

In vivo treatments

Surgical castration was performed on 8-week-old $Pten^{pc-/-}$ mice and, for allografts, when tumors were approximately 100 mm^3, under anesthesia with isoflurane as previously described.[4]

When specified, enzalutamide (APExBio, cat. MDV3100) was administered on a Monday through Friday schedule by oral gavage (30mg/kg); anti-IL-23 monoclonal antibody (clone G23-8; eBioscience™) and Rat IgG1 kappa Isotype Control (eBRG1; eBioscience) were intraperitoneally injected twice a week (100μg/mouse). αCXCR2 (AZD5069; AstraZeneca) was administered with daily intraperitoneal injections at a final concentration of 100 mg/kg on a Monday through Friday schedule. Based on tumor growth curves, early phase of therapy response was defined as the first two weeks of treatment.

Rivaroxaban (BAY 59-7939; Selleck Chemicals S3002) was administered on a Monday through Friday schedule by oral gavage (5 mg/kg), at least 4 hours later enzalutamide administration. LMWH (Dalteparin) was administered subcutaneously daily (200 IE/Kg) on the dorsal back of the mice. *In vitro*-derived hMDSCs were intraperitoneally injected twice a week (1.5 $x10^6$/mouse) in LNCaP-tumor bearing mice. Mice were routinary weighted and checked for their behavior. Animals were allocated randomly to each treatment group.

Bone marrow reconstitution

Bone marrow reconstitution with $F10^{fl/fl}$ precursors was performed on 6-week-old $Pten^{pc-/-}$ mice. Recipient $Pten^{pc-/-}$ mice were lethally irradiated (900 rad) and transplanted i.v. two hours later with 1 x 10^7 viable bone marrow cells from either $F10^{fl/fl}$; $LysM\text{-}Cre^+$ or $F10^{fl/fl}$; $LysM\text{-}Cre^-$ mice. Bone marrow were flushed under sterile conditions with PBS using a 21-gauge needle. Red blood cells were removed by using ACK lysing buffer (Gibco; A1049201) and cell suspensions were filtered and checked for viability using trypan blue.

Bulk RNA-sequencing analysis

Mouse prostate tumor tissues were quickly excised and homogenized for RNA extraction. RNA was extracted using TRIzol RNA isolation reagent (Invitrogen, Cat n=15596026), followed by RNase-Free DNase set (Qiagen, Cat n=79254) treatment, following manufacturers' guidelines. RNA integrity was checked with Agilent 2100 Bioanalyzer system. NEBNext® Ultra™ II Directional RNA Library Prep with Sample Purification Beads (New England BioLabs Inc) and NEBNext poly (A) mRNA magnetic isolation module (New England BioLabs Inc) were used for cDNA synthesis. The libraries were sequenced using the NextSeq 2000 and P2 kit High (100 cycles; Illumina). Samples were processed starting from stranded, single-ended 120bp-long sequencing reads.

RNA from IVD-hMDSCs was extracted using RNeasy Micro Kit (Qiagen, Cat n=74004), following manufacturers' guidelines. RNA integrity was checked with Agilent 2100 Bioanalyzer system. NEBNext UltraExpress™ RNA Library Prep Kit (New England BioLabs Inc,) and NEBNext poly (A) mRNA magnetic isolation module (New England BioLabs Inc) were used for cDNA synthesis. The libraries were sequenced using the NextSeq 2000 and P2 kit High (100 cycles; Illumina). Samples were processed starting from stranded, single-ended 120bp-long sequencing reads.

STAR (v2.7.10a)[84] was used for sequence alignments. Bulk RNAseq data of $Pten^{pc-/-}$ tumors from mice reconstituted with bone marrow precursors from either $F10^{fl/fl}$; $LysM\text{-}Cre^+$ or $F10^{fl/fl}$; $LysM\text{-}Cre^-$ mice were aligned to mouse genome (GRCm38), whereas, bulk RNAseq data from human IVD-hMDSCs treated or not with recombinant CD84 were aligned to human genome (GRCh38).

Genes with zero expression in all samples were removed and DESeq2[88] (alpha = 0.05 and Independent Filtering feature= T) was used to obtain differentially expressed genes. Gene-set enrichment analysis was performed on Hallmark. Collection using fgsea package.[90]

Single – cell RNA-sequencing analysis

Prostate tumors were resected from either 10-week-old, sham-operated (hormone-sensitive, HS) or castration-resistant (16 weeks after surgical castration, CR) 24-week-old $Pten^{pc-/-}$ mice. All prostate lobes were collected and processed to obtain a single-cell suspension. TRAMP-C1 allografts were resected from C57/BL6N-tumor bearing mice either 12 days (Early phase) or 24 days (Late phase) after the initiation of the treatment. Enzalutamide, Enzalutamide + anti-IL-23 and Enzalutamide + aCXCR2 therapies were started the day after surgical castration.

For single-cell RNAseq, tissues were digested in Digestion Buffer composed by RPMI 1640 Normal medium, Collagenase D (5 μg/mL) and DNAse (100 U/mL), in the presence of RNase Inhibitor Murine (New England Biolabs). The cell suspension was incubated for 40 min at 37°C on a rocker. The digestion was stopped adding normal medium and cell suspension was filtered by a 100 μm cell strainer and kept on ice for 4 min. After further filtering, cell suspension was spun down at 1500 rpm for 5 min at 4°C and cell subsets were enriched by FACS sorting. Flow Cytometry staining of tumors was performed using the following antibodies: anti-Epcam-FITC (clone G8.8), anti-CD45-bv605 (clone 30-F11), and anti-CD11b-bv421 (clone M1/70); and anti-Gr1-APC (clone RB6-8C5), and 7AAD (eBioscience). For $Pten^{pc-/-}$prostate samples, the 7AAD negative cells were sorted: i) $Epcam^{+-}$ $CD45^{-}$, ii) $Epcam^{-}$ $CD45^{+}$ $CD11b^{+}$ $Gr1^{+}$; iii) $Epcam^{-}$ $CD45^{+}$ $CD11b^{-}$ $Gr1^{-}$. For TRAMPC-1 allografts, the 7AAD negative cells were sorted as follows: i) $CD45^{+}$ $CD11b^{+}$ $Gr1^{+}$; ii) $CD45^{+}$ $CD11b^{-}$ $Gr1^{-}$; iii) $CD45^{-}$. After counting, cells were mixed together in ratio 1:1:1 to perform single-cells sequencing.

Single-cell suspensions were processed with Single Cell 3′ Reagent Kit v3 (Chromium Single Cell 3′ Library & Gel Bead Kit v3, Chromium Single Cell G Chip Kit, 10x Genomics) and Chromium Controller (10x Genomics) according to the protocol at the BIOS+ Genomics Facility in Bellinzona. The generated libraries were sequenced using Illumina NextSeq500 Systems accordingly with the 10x Genomics manual.

Sequencing data were processed by CellRanger (version 3.1.0) and reads were aligned to mouse genome (mm10 v3.0.0) with STAR (v.2.7.10a). To reduce the 'dropout' phenomenon, RMagic package was used on gene-counts.[85]

To filter the cells, we removed those that had more than 25% expression on mitochondrial genes, fewer than 100 total genes expressed and we considered only protein-coding genes defined using getBM (biomaRt package).[89] All the samples were integrated using Seurat package[86] (FindIntegrationAnchors and IntegrateData functions). Principal component analysis (PCA) dimensionality reduction considered the top 2000 most variable features identified. Moreover, the dimensional reduction technique t-distributed stochastic neighbor embedding (t-SNE) and UMAP were applied using the RunTSNE and RunUMAP functions from Seurat.[86]

Differentially expressed genes (DEGs) were identified using FindAllMarkers or FindMarker functions (test.use=MAST). Genes were identified as differentially expressed in a particular set of cells if FDR < 0.05 and minimum expression in at least 30% of cells.

Common PMN-MDSCs secreted factors between the two mouse models were identified using the list of Human Protein Atlas (https://www.proteinatlas.org). Expression of genes was visualized using the VlnPlot, DotPlot or FeaturePlot functions. All graphs were performed using Seurat[86] package, ggplot2 package and pheatmap package.

Human sc-RNA seq data were downloaded from GEO (GSE181294 [32]) and analyzed with the same pipeline described above.

F10^{high}/CD84/PMN signature

To identify *F10^{high}* PMNs in PCa bulk RNA-seq datasets, we generated a *F10^{high}*/*CD84*/PMN signature, as follows; starting from single-cell RNA-seq analysis of *Pten$^{pc-/-}$* and TRAMP-C1 CR tumors we identified a list of genes commonly upregulated in the *F10^{high}* PMNs as compared with *F10^{low}* in both models. Next, by analyzing bulk RNA-seq data of human IVD-hMDSCs treated with hrCD84 as compared with the untreated ones, we selected the significantly upregulated genes upon CD84 ligation in human PMNs. Then, we analyzed mouse *F10^{high}* PMNs and human IVD-MDSCs stimulated with CD84 and found only six genes, namely *SPP1*, *SLC2A1*, *RSRP1*, *TFRC*, *EGLN3*, *SLC26A1*, commonly upregulated in the *F10^{high}* subset independently from the organism. Finally, we combined these six genes together with four unique markers of human PMNs (*ITGAM*, *CD33*, *FUT4*, *CD14*), *F10* and *CD84* to define the *F10^{high}*/*CD84*/PMN signature. Kaplan-Meier curve for disease free survival in the TCGA dataset of PCa patient was then generated by stratifying the patients based on GSVA-score[87] of *F10^{high}*/*CD84*/PMN signature. In particular, with HIGH we selected patients belonging to the third tertile, while with LOW, the others. Kaplan-Meier curve for overall survival in the SU2C and RMH datasets of mCRPC patients was generated by stratifying the patients based on GSVA-score[87] of *F10^{high}*/*CD84*/PMN signature. HIGH and LOW were defined using the Maxstat method.[98,99]

Bioinformatic analysis of PCa RNA-seq data

For mouse, RNA-seq data from wild-type and *Pten$^{pc-/-}$* mice were used from previous paper of Alimonti's group.[81] For human samples, almost 1200 bulk RNA-seq samples were downloaded from a recent paper by Bolis et al.,[58] comprehensive of normal, primary and CRPC human samples. We checked the expression of different genes and various signatures of interest calculated using GSVA[87] (method = "ssgsea") package. The PMN-MDSCs signatures evaluated included: PMN-MDSCs signature 1, a PMN-MDSCs signature described by Veglia et al.[59]; PMN-MDSCs signature 2, a short list of canonical markers (*ITGAM, CD33, CD14, FUT4*);

PMN-MDSCs signature 3, an enriched list of canonical markers of PMN-MDSCs activation.[51,100] Senescent_PMNs signature was derived from Bancaro et al.,[10] whilst signatures of aged or mature neutrophils were defined as previously described.[49,50,52]

Kaplan-Meier curves for overall survival from the time of CRPC biopsy were generated by stratifying PCa patients using the Maxstat method[98,99] on the basis of their expression levels of the *F10^{high}/CD84*/PMN signature from either the RMH (n=94)[80] or SU2C/PCF (n=141)[38] patients, cohorts. AR activity score is an accumulation measurement of AR pathway activity based on 43 genes regulated by AR in PCa cell lines and metastatic PCa.[78]

Flow cytometry and analysis

Mouse and human tumors were disaggregated and digested in Collagenase D (5 μg/ml) and DNase (100 U/ml) for 45 minutes at 37°C on rotation to obtain single-cell suspension. Cells were first stained with FVS BD Horizon™ Fixable Viability Stain 440UV for viability (BD; 566332). After neutralization of unspecific binding with anti-CD16/CD32 (clone 93), single-cell suspensions were stained with specific mAb (primary antibodies directly conjugated) to assess the phenotype. The antibodies used were: anti-CD45 (clone 30-F11); anti-CD3 (clone17A2); anti-CD8a (clone 53-6.7); anti-CD4 (clone RM4.5); anti-CD19 (1D3); anti-B220 (RA3-6B2); anti-NK1.1 (clone PK136); anti-CD49b (HMα2); anti-CD11b (clone M1/70); anti-Ly-6G (clone 1A8); anti-Ly6C (clone HK1.4); anti-IL-23p19 (clonefc23cpg); anti-CXCR2 (clone V48-2310); anti-F4/80 (clone T45-2342); anti-CD103 (clone M290); anti-CD84 (clone mCD84.7); anti-CD11c (clone N418); anti MHCII (cloneM5/114.15.2). All the antibodies were purchased from eBioscience or Biolegend or R&D or BD. Staining of mouse samples for FX was performed using a polyclonal anti-FX Factor X antibody (Genetex, GTX110300), and appropriate anti-Rabbit IgG (H&L) - Alexa Fluor™ 647 or anti-Rabbit IgG (H&L) - Alexa Fluor™ 488 secondary antibody (Thermo Scientific).

Human tumors were disaggregated and digested in Collagenase D (5 μg/ml) and DNase I (100 U/ml) for 30 min at 37°C to obtain single-cell suspensions. Single-cell suspensions were stained with specific monoclonal antibodies (primary antibodies directly conjugated) to assess the phenotype. The antibodies used were: CD45 (clone HI30), CD33 (clone WM-53), CD11b (clone M1/70), CD14 (clone 63D3), CD15 (clone HI98), CD84 (clone CD84.1.21), Human BD Fc Block™ (Clone Fc1-RUO). All the antibodies were purchased from eBioscience or Biolegend or R&D or BD. Anti-FX (f21-4.2)-488 labeled antibody was kindly provided by Wolfram Ruf.[76]

Samples were acquired using a FACSymphony™ A5 (BD Biosciences) and analyzed using FlowJo software (BD Biosciences).[83] 28-Parameter Flow Cytometry Standard (FCS) 3.0 files were imported into FlowJo software version 10 and left untreated or biexponentially transformed (the same transformation for all files, performed in version 10) prior to UMAP analysis. Following transformation, 28-Flow Cytometry Standard (FCS) 3.0 files were assigned with a computational barcode for their unique identification, concatenated and visualized with UMAP ("https://arxiv.org/abs/1802.03426") in FlowJo. The following parameters were used: Euclidean; nearest neighbors: 10; minimum distance: 0.11; number of components: 2. All parameters except for CD45 and Fixable viability Staining as dead cell marker, were included in the analysis. The clusterization was automatically defined by the X-Shift algorithm. The default parameters were used to run the algorithm except for the K-nearest neighbor value set at 250 to reduce the number of clusters. The identity of the clusters was determined by the heatmap generated by Cluster explorer.[101,102]

Immunohistochemistry and immunofluorescence

For immunohistochemistry (IHC), tissues were fixed in 10% formalin (Thermo Scientific, 5701) and embedded in paraffin in accordance with standard procedures. Preceding immunohistochemical staining, tumor sections (4μm) were exposed to two washes with OTTIX plus solution (Diapath, X0076) and subsequent hydration with OTTIX shaper solution (Diapath, X0096) followed by deionized water. Antigen unmasking was performed by heating sections in the respective pH solutions based on the antibodies used at 98°C for 20 minutes. Subsequently, the sections were blocked for peroxidases and nonspecific binding of antibodies using 3% H2O2 (VWR chemicals, 23615.248) and Protein- Block solution (DAKO Agilent technologies, X0909) respectively for 10 mins each split by 0.5% PBST washing. H&E staining was performed according to standard procedures. Sections were stained with anti-Ki67 (Clone SP6; Histocom), anti-Cleaved Caspase 3 (Cell signaling #9661), anti-p16 (Abcam #ab211542) antibodies.[103] Images were scanned with Aperio and analyzed with ImageScope v12.3.2.8013 (Leica Biosystem). For PAR2 immunohistochemical evaluation a four-point system was utilized, where score 0 = no stain; score 1 = faint stain in $\geq 1 \leq 30$ % of cells; score 2: faint or moderate stain in $>30 \leq 70$ % of cells; score3: strong stain in ≥ 71 % of cells. Patients who had already undergone radical prostatectomy for localized PCa were stratified based on PAR2 score as negative (Score 0, +1), moderate (Score 2+) and high (Score 3+) PAR2. Survival analysis (DFS) at a median follow-up of 114 months was performed using survival and survminer packages.

For immunofluorescence, BM-MDSCs were seeded on coverslips and fixed with 4% PFA for 10 mins before staining. Then cells were permeabilized with Tween 0.1% for 10 min, washed twice with 1xPBST (0.1% Tween 20), and incubated with blocking solution (10 % FBS in 1xPBST). Sections were stained with Factor X antibody (Genetex, GTX110300) at 4°C overnight, followed by 3 washes with 1xPBST. Alexa Fluor 488-conjugated anti-rabbit IgG secondary antibody (Thermo Scientific, cat # A-11008), anti-CD11b 594 (clone M1/70; Biolegend, cat # 101254), were incubated at room temperature for 1 hour. The nuclei were counterstained with Hoechst 33342 1μg/ml (Invitrogen, cat # H3570) and slides were mounted with ProLong (Invitrogen, cat # P36931). Images were acquired by a confocal microscope Leica SP5, with an oil-immersion objective (63×/1.4 NA Plan-Apochromat; Olympus), using laser excitation at 405, 488, or 594 nm. Images were processed using ImageJ software.

RNAish

For RNAish, tissues were fixed in 10% formalin (Thermo Scientific, 5701) and embedded in paraffin in accordance with standard procedures. RNAish for human *F10* was performed according to the manufacturer's protocol (RNAscope Multiplex Fluorescent Reagent Kit v2 Assay) with minor adaptations followed by an IF staining for CD15. After the inclusion of the organs in paraffin, were cut into sequential sections of 4 μm and then baked in a dry oven at 60°C for 1 hour. The slides were then deparaffinized using two steps of 5 min in OTTIX Plus (Diapath, X0076) and one Step of 5 min in OTTIX Shaper (Diapath, X0096). For the pretreatment steps, the sections were covered for 10 min at RT with RNAscope Hydrogen Peroxide, incubated for 15 min in RNAscope Target retrieval reagent (ACDBio 322000), and then treated 30 min at 40°C with RNAscope Protease Plus (RNAscope H2O2 and protease reagents ACDBio Cat 322381).

The FX-C2 probe (1:50 ACDBio 1333641-C2) was prepared according to the manufacturer's protocol and used to incubate the samples for 2h at 40°C. The following steps of amplification and development of the signal were also performed following exactly the RNAscope Multiplex Fluorescent Reagent Kit v2 Assay protocol (ACDBio Cat 323110). TSA Vivid 650 fluorophore was used for *F10* detection (1:1000 ACDBio 323273). Once completed the RNAscope protocol, but prior to DAPI staining, IF for CD15 was performed. All the steps of the IF staining were done at RT and avoiding the direct light exposure as follows: after 30 min in Protein blocking buffer (DAKO X0909) the samples were incubated for 90 min with CD15 (1:100 Cell Signaling #4744) and, after two wash steps in PBS-Tween, with anti-rabbit IgG AF594 (1:400 Invitrogen #A11012) for 30 min. After nuclear counterstaining with DAPI (RNAscope Multiplex FL v2 DAPI ACDBio RTU Cat #323110), the slides were mounted with Fluoromount-G (Invitrogen 00-4958-02) and air dried for 30 min at RT. Images were acquired using a confocal Leica Stellaris SP8 microscope with a Leica HCX PL APO lambda blue 40 × 1.40 OIL UV objective and the Leica LAS X software. The threshold for *F10* RNAish was set to 3 puncta/cell. A constant area of 0.38 mm^2 was analyzed per each sample.

Quantification of plasma levels of FX in CRPC patients and survival analysis

Plasma samples were obtained from 106 patients with mCRPC. Clinical data, including hematology, biochemistry, PSA, and other prognostic factors for PCa were retrospectively collected from the hospital electronic medical record system. 106 patients had hematology results available for analyses but one or more of the prognostic factors were missing from 17 patients, leaving 89 patients for the multivariable survival analyses. Results from hematology and biochemistry samples taken at the closest available time point to the plasma samples (within 14 days) were obtained. PSA results obtained at the closest available time point to the plasma samples (within 6 weeks) were obtained. Plasma levels of FX were quantified by using the Human Coagulation Factor X ELISA Kit from Novus Biologicals (NBP2-60625) following manufacturer's instructions.

Overall survival was calculated from the date of serum sample collection for measurement of serum FX level to the date of death or the date of last follow-up/contact (data cut-off: 1st Dec 2022). Overall survival analyses were performed using the Kaplan-Meier method. Univariate analysis of the association between FX level and overall survival from the time of serum collection was performed using Cox proportional hazards models. Multivariable analysis of the associations between overall survival from the time of serum collection was performed and covariates including Gleason Score, PSA, lactate dehydrogenase, albumin, hemoglobin, alkaline phosphatase, and the presence of metastatic disease (M1 status) at diagnosis were performed using Cox proportional hazard models. Non-parametric variables were log-transformed. Pearson correlation and linear regression were used to measure associations between blood neutrophil count, NLR and plasma FX level. All analyses were conducted using R version 2022.07.2.

Statistical analysis

For ethical reasons, the minimum number of animals necessary to achieve the scientific objectives was used. Animals were allocated randomly to each treatment group. Different treatment groups were processed identically and animals in different treatment groups were exposed to the same environment. For FACS, RNAish, IF and IHC analysis, there were no pre-established criteria for sample exclusion, except evident insufficient sample quantity and/or poor histological quality.

All statistical analyses were performed using GraphPad Prism 8, or R-Studio. Shapiro-WilK normality test was performed to analyze data distribution. Statistically significant differences between control and experimental groups were determined using either the Student's t-test or the Mann-Whitney test, according to the data distribution. For multiple comparisons, either one-way ANOVA or two-way ANOVA tests were performed, followed by the appropriate post-hoc test, as indicated in figure legends. For bioinformatic analyses, the data were considered statistically significant with FDR<0.05. All the statistical details of experiments, including number of animals, number of experimental replicates, and the statistical test used, can be found in the figure legends. Differences were considered significant when $p \leq 0.05$ and are indicated in figures as following: * $p \leq 0.05$, ** $p < 0.01$, *** $p < 0.001$, **** $p < 0.0001$.